J. Fluid Mech. (1993), *vol.* 246, *pp.* 163–195

An experimental study of vortex shedding behind linearly tapered cylinders at low Reynolds number

By PAUL S. PICCIRILLO AND C. W. VAN ATTA†

Department of Applied Mechanics and Engineering Sciences, University of California, San Diego, La Jolla, CA 92093, USA

(Received 10 November 1990 and in revised form 19 June 1992)

Experiments were performed to study vortex shedding behind a linearly tapered cylinder. Four cylinders were used, with taper ratios varying from 50:1 to 100:1. The cylinders were each run at four different velocities, adjusted to cover the range of laminar vortex shedding for a non-tapered cylinder. The flow was confirmed to consist of discrete shedding cells, each with a constant frequency. For a centrespan Reynolds number greater than 100, the dimensionless mean cell length was found to be a constant. Individual cell size was found to be roughly self-similar. New shedding cells were created on the ends of the cylinders, or in regions adjacent to areas not shedding. Successful scalings were found for both the cell shedding frequencies and their differences, the modulation frequencies. The modulation frequencies were found to be constant along the cylinder span. The shedding frequency Strouhal number versus Reynolds number curve was found to have a slightly steeper slope than the Strouhal number curve for a non-tapered cylinder. Vortex shedding was found to begin at a local Reynolds number of about 60, regardless of any other factors. End effects were found to be of little importance.

The vortex splits, which form the links between shedding cells, were found to be similar in some respects to those found by earlier investigators. Amplitude results suggested that the splits at different spanwise locations are temporally sequenced by an overall flow mechanism, a supposition confirmed by flow visualization. Wavelet analysis results showed that while the behaviour of the shedding frequencies in time was relatively unaffected by changing taper ratio, the behaviour of the modulation frequency in time was greatly affected. Comparisons with other experiments point out the universality of vortex splitting phenomena.

1. Introduction

The study of vortex shedding behind bluff bodies has a long and rich history. However, most of the work done in this area has been concerned with bluff bodies of spanwise-uniform cross-section. In this paper, the flow behind a cylindrical bluff body with non-uniform diameter, a linearly tapered cylinder, will be examined.

The study of vortex shedding behind a linearly tapered cylinder was initiated by Gaster, in two papers (1969, 1971). In the first, Gaster described flow past tapered cylinders with taper ratios (he defined taper ratio, $R_T = l/(d_2 - d_1)$, where l is the cylinder length, and d_1 and d_2 are the diameters of the narrow and wide ends of the cylinder, respectively) of 18:1 and 36:1, in a water tunnel. He discovered that

† Also at Scripps Institution of Oceanography.

the fluctuating velocity in the wake was not singly periodic in time, as for a straight cylinder, but rather was a combination of two frequencies, one approximately an order of magnitude lower than the other. This modulated signal appeared at all spanwise locations behind both of his cylinders, at all Reynolds numbers between 66 and 172. He suggested that the modulation frequency was a constant along the span of the cylinder. In his second paper (1971), Gaster described the flow behind a more mildly tapered cylinder (R_T of 120:1) in a wind tunnel. He found that the flow in this case was cellular in nature, i.e. composed of spanwise cells of constant shedding frequency.

Van Atta & Piccirillo (1990) also found cellular structure behind cylinders with roughly the same taper as those used first by Gaster (R_T of 13:1, 23:1, and 32:1). Further, Van Atta & Piccirillo showed that the difference in shedding frequencies between adjacent spanwise cells was a constant. This frequency difference was found to correspond to the lower (modulation) frequency first seen by Gaster. Piccirillo (1990) was able to show that the cause of this modulation frequency was a vortex splitting process, whereby one vortex line would break into two, at the boundary between two cells.

Recently, Noack, Ohle & Eckelmann (1991) have proposed a theoretical model for the tapered cylinder based on coupled nonlinear oscillators, and described a physical experiment on a cylinder with R_T of 90:1 and an aspect ratio of 90:1. This flow showed the behaviour described above. Jespersen & Levit (1991) have studied the problem numerically, with conditions set to match the cylinder of 100:1 taper ratio of this study with a free-stream velocity of 0.5 m/s.

Similar results are contained in the work of Maull & Young (1973), Griffin (1987), and Woo, Cermak & Peterka (1989), who find cellular behaviour in shear flow past uniform bluff bodies. Other similar results can be found in the work of Gerich & Eckelmann (1982), who discovered that in the flow behind straight cylinders, there exist 'end cells', with shedding frequencies about 15% lower than the main shedding frequency of the cylinder, at each end of the cylinder. Similar results have been obtained by Slaouti & Gerrard (1981). Eisenlohr & Eckelmann (1989) and Williamson (1989) have both looked carefully at the end cells in their experiments and found that they connect to the main vortex shedding region by means of a vortex splitting process. Williamson has also found that, for certain end conditions, this vortex splitting process can be seen all along the span of the cylinder. Browand & Troutt (1985) have found similar 'vortex dislocations' in a free shear layer, which were also seen when the shear layer was forced (Browand & Prost-Domasky 1990). Evidence for vortex splitting phenomena has also been seen by Lewis & Gharib (1992) in the wake of a cylinder with a discontinuity in diameter. In their work, two different modes of interaction, and thus two different types of vortex splits, were found between the two parts of the cylinder, each with own vortex splitting 'pattern'.

The flow behind linearly tapered cylinders is an excellent example of a flow with a generically simple three-dimensionality, especially in the case of cylinders with mild taper (R_T of 50:1 or more). The small amount of taper compared to the length of the cylinder makes this flow an ideal one to begin to understand the flows behind general three-dimensional bluff bodies. In this flow, the three-dimensional vortex interactions might be expected to occur in well-defined and clearly visible patterns. This experiment thus serves as a starting point for the study of vortex shedding behind more complex three-dimensional bodies.

In the present work, we studied both the nature of the overall flow and the details of the vortex split, looking at both its cause and its effects on the flow. We considered

the effects of changing taper ratio, endplate configuration, and flow velocity. Section 2 presents a brief description of the experiments performed. The results of the experiments are presented in the next section. First, the overall flow is discussed, followed by a detailed description of the vortex split. In §4, comparisons with similar experiments are made, and conclusions are drawn in §5.

2. Experimental method and set-up

The experiments in air were performed in the AMES Geophysical Fluid Dynamics wind tunnel, using a 76×76 cm test section. The mean velocity, U, in the tunnel was varied from 0.3 to 0.6 m/s. Four tapered cylinders were used in the experiments. All were 15 cm long, with diameters varying linearly along their spans. The taper ratios of the cylinders were 100:1, 75:1, 60:1, and 50:1. A 0.33 cm diameter straight cylinder was also tested, for comparison with our tapered cylinder results. Each of the cylinders was run at four different speeds, to span the Reynolds number range for regular vortex shedding behind a non-tapered cylinder. These runs are summarized in table 1. For convenience, the naming convention used in this table will be used for the rest of the paper. In order to determine the influence of end conditions, three types of endplates were tested on the 100:1 tapered cylinder (which was expected to be most susceptible to end effects) and the straight cylinder: (i) 7.5 cm diameter circular endplates, (ii) 3.75 cm diameter circular endplates, and (iii) flush-fitting 'nubs' similar to the spacers used by Eisenlohr & Eckelmann, but with each 'nub' tapered so that it had a flush fit to one end of the tapered cylinder. The cylinder was held in place by two airfoil-shaped supports attached to a plate which was mounted on the side wall of the test section.

Two types of experiments were performed in the wind tunnel: (i) smoke-wire flow visualization and (ii) hot-wire anemometry. The flow visualization was performed using a 0.025 cm diameter Nichrome wire and model-train smoke fluid to create the smoke. The wire was placed $2d_m$ behind the cylinder, where d_m is defined as 0.33 cm, roughly the mean diameter of the tapered cylinders used in the experiments, and offset $1d_m$ from the cylinder centreline, in order to record only one side of the vortex street shed from the cylinder. The wire, the flash used for illumination, and the Nikon F3 camera used for the photography were controlled by an IBM-PC clone.

The hot-wire anemometry was performed using a rake of 4 Dantec 55P11 single-wire hot wires. The spanwise, or z-direction, separation between the wires was varied from 0.33 to 1.33 cm, with a value of 0.66 cm being the standard separation. The wires were located $2d_m$ downstream, offset by $1d_m$ from the centreline of the cylinder. The wires were positioned using a three-axis Velmex, Inc. traverse and run by an IBM-PC clone. A sketch of the hot-wire set-up, showing the axis conventions used in the experiments, is shown in figure 1.

The hot-wire signals were sent to a Masscomp 6000 computer, where they were digitized and stored for processing. Most of the data records were 10 s long and were sampled at a rate of 1500 Hz, giving 15000 data points per channel per record. The high sampling rate was chosen to allow the data to be filtered and then desampled before making power spectral estimates.

A series of flow visualization experiments in water were performed in the UCSD Geophysical Fluid Dynamics water tunnel. The cylinders and support airfoils used in the wind tunnel experiments were re-used. Only the 'nubs' described above were used as endplates. The mean velocity U was approximately 6 cm/s. For the visualization, the cylinders were painted with a mixture of fluorescein and natural

Cylinder R_T	Velocity (m/s)	*Re* small end	*Re* large end	Run number
100:1	0.298	54	87	11
	0.400	73	116	12
	0.505	91	145	13
	0.596	111	178	14
75:1	0.316	57	103	21
	0.400	73	131	22
	0.499	91	163	23
	0.547	99	179	24
60:1	0.316	57	115	31
	0.371	67	135	32
	0.421	76	153	33
	0.494	90	179	34
50:1	0.298	32	97	41
	0.365	40	119	42
	0.447	49	146	43
	0.547	60	179	44

TABLE 1. Configurations used in the basic experiments

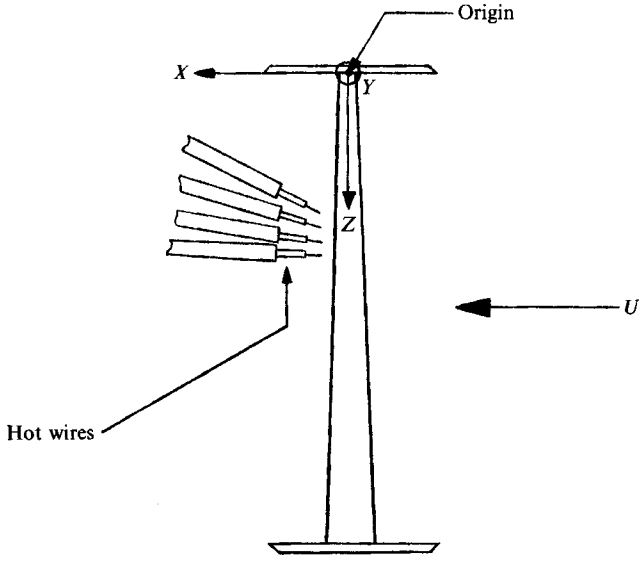

FIGURE 1. Schematic of the hot-wire set-up used in the experiments, with axis conventions shown.

oils which dissolved slowly in water. This mixture, when washed off the cylinder, was illuminated by a laser sheet produced by a Coherent Innova 70 argon-ion laser. The sheet was oriented either along the spanwise axis of the cylinder, or perpendicular to it. The illuminated flow produced by the sheet was recorded on videotape using a Sony XC-77RR CCD camera.

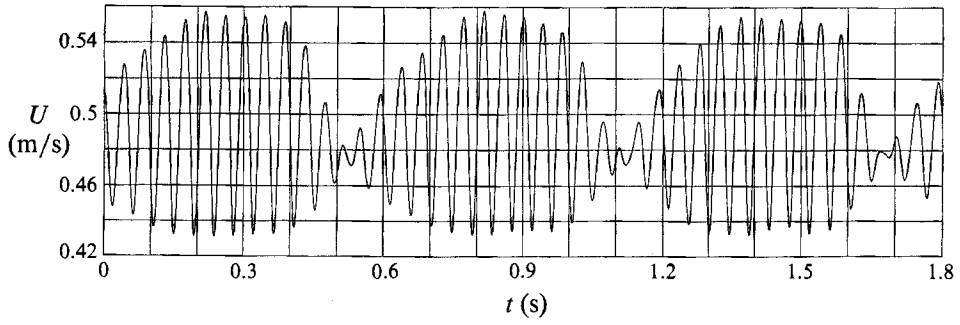

FIGURE 2. A typical velocity time-history plot.

3. Experimental results

3.1. *The behaviour of the shedding cells*

A typical velocity time-history plot is shown in figure 2. The plot clearly shows the modulated signal behaviour observed by Gaster, Van Atta & Piccirillo, and Noack *et al.* All of the velocity plots examined were qualitatively similar to the one shown in the figure. Quantitative differences did exist, however, which will be discussed later in the paper.

Spectra were examined next, in order to decide if the flow was indeed cellular in nature, and, if so, where the cell boundaries lay. A typical result of this investigation is shown in figure 3. In this plot, the two power spectral plots come from adjacent spanwise stations separated by $\Delta Z = 0.66$ cm. Each spectrum has three primary peaks, at 25.63, 24.02, and 1.61 Hz. The 1.61 Hz peak is the modulation frequency, which is the difference between the two shedding frequencies. In the first plot, the 25.63 Hz peak is clearly dominant, while in the second plot, obtained closer to the large-diameter end of the cylinder, the 24.02 Hz peak is dominant. This rapid switch of dominant spectral peaks over such a short spanwise distance immediately suggests that the two stations are in different shedding cells, and that a vortex splitting process similar to that seen by Williamson is involved. Also, note that there are no dominant frequencies other than the two shedding frequencies, the modulation frequency, and harmonics and sums thereof.

Shedding cell boundaries were determined from the spectra, by either finding a location where two shedding frequencies were equal in magnitude, or, more commonly, taking the midpoint between two adjacent measuring stations with different primary shedding peaks. The spanwise locations of the cell boundaries were found to vary somewhat from run to run. For the 100:1 cylinder with $U = 0.5$ cm/s, the positions of the cell boundaries changed by up to 1.0 cm, when nominally identical runs were compared. From this, it seems clear that the cell boundaries can change from one realization of the flow to another. Therefore, care was taken when using the cell boundary positions in quantitative analysis.

In figure 4, the number of cells N found for each cylinder is plotted against cylinder centrespan Reynolds number, Re_{cs}. The points marked with arrows represent runs in which the cylinders were not shedding vortices along their entire length. N initially increases with increasing Re_{cs}, but then tends to level off at a constant value, usually when the cylinder begins shedding along its entire length. N also increases with decreasing taper ratio (increasing amount of taper).

To determine where the new cells were being created as the Reynolds number was

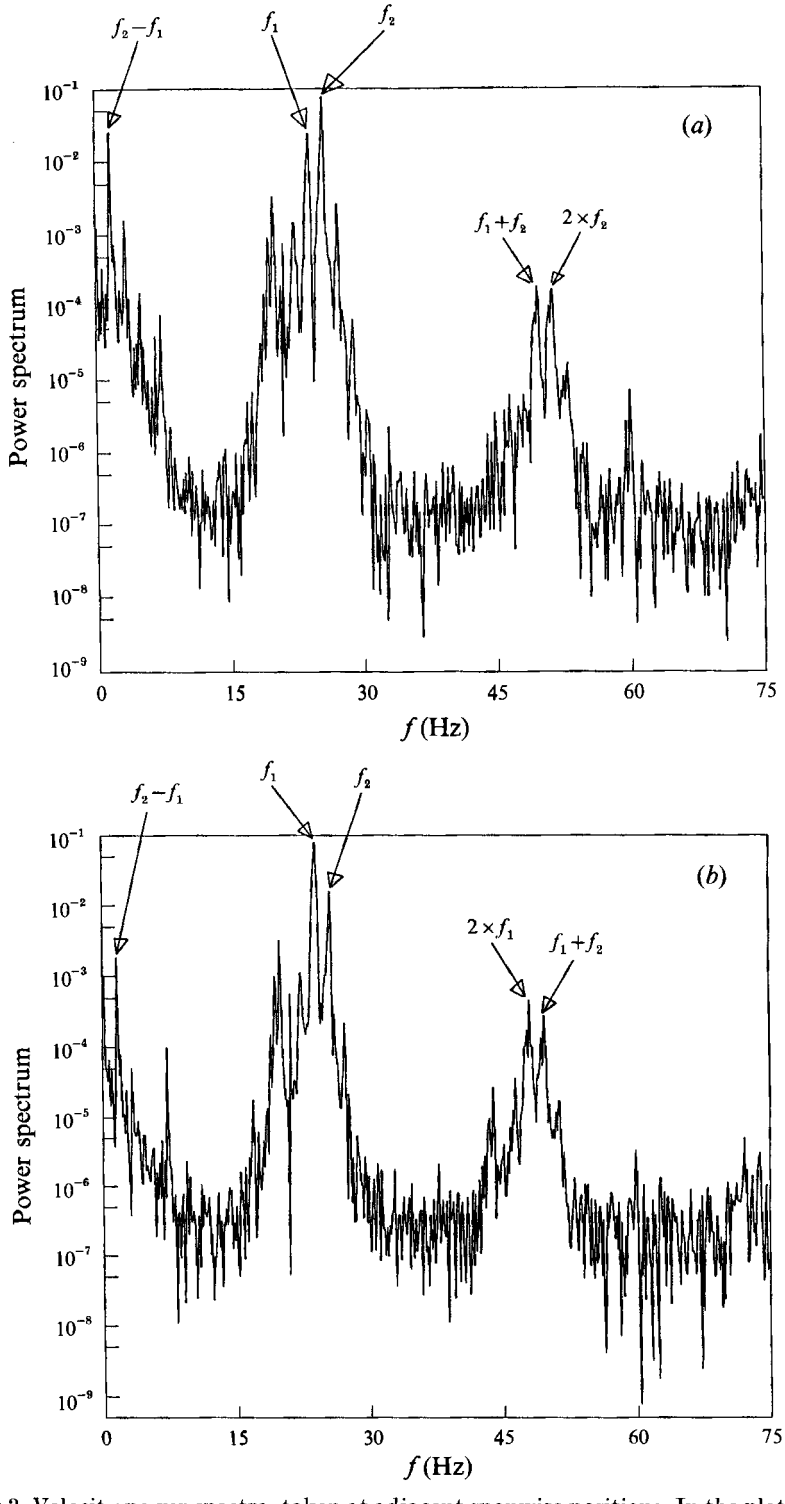

FIGURE 3. Velocity power spectra, taken at adjacent spanwise positions. In the plots, $f_1 = 24.02$ Hz and $f_2 = 25.63$ Hz. (*a*) $Z = 4.2$ cm; (*b*) $Z = 4.9$ cm.

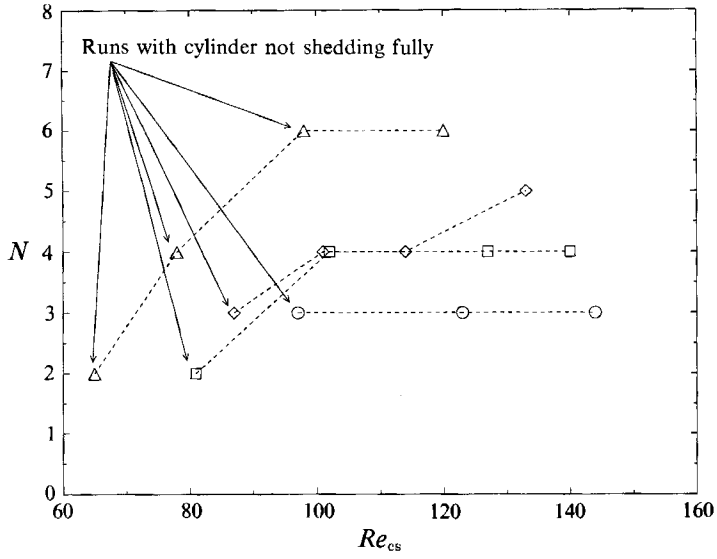

FIGURE 4. Number of shedding cells for all the cylinders, plotted against centrespan Reynolds number. ○---○, 100:1 cylinder; □---□, 75:1; ◇---◇, 60:1; △---△, 50:1.

increased, the cell midpoint positions were plotted for each run. The results for the 75:1, 60:1, and 50:1 R_T cylinders, which have a changing number of cells, are shown in figure 5. Here, we see that the cells are being created at the ends of the cylinder, or, in the case where the cylinder is not shedding fully (areas not shedding are marked on the plots), at the end of the shedding region adjacent to the region with no shedding. As a corollary to this, we notice that the end cells (also marked on the plots) are of somewhat varying size. This suggests that the end cells fill space at the ends of the cylinders when a discrete number of cells will not completely fill the cylinder. When an end cell becomes as large as a shedding cell, another shedding cell is then created to fill the space, and the end cell is reduced in size, or even eliminated. This in turn suggests that the influence of end effects on the main body of the flow is small, as the end cell seems to be acting more as a place holder than as a dynamically important part of the overall flow.

Looking at figure 5, it is clear that the cells are not of uniform size along the span of the cylinders. In figure 6, we plot the cell length $l_c = z_{\text{end 1}} - z_{\text{end 2}}$ versus spanwise position for all the cells not influenced by end effects, i.e. not next to an end cell or the end of the cylinder (the latter types of cells were found to vary greatly in length). The cell size l_c clearly increases with local diameter. If one supposes that the taper ratio is the governing geometric parameter of the flow, it is logical to assume that the cell size would scale according to a self-similarity hypothesis, namely, that cell length would be proportional to local diameter of the cylinder at the cell midpoint. In each plot, a self-similar line, shown as a dashed line, is shown for comparison with the data. The constant of proportionality for each of these lines was chosen to fit the data. The majority of the cell sizes are consistent with the self-similarity hypothesis, within the uncertainty due to the run-to-run variation in cell boundary positions.

An attempt was made to scale the mean cell length for all the cylinders. The mean cell size was computed for each run, using all the cells, not just the ones deemed free of end effects, and then non-dimensionalized by recasting it in terms of the change

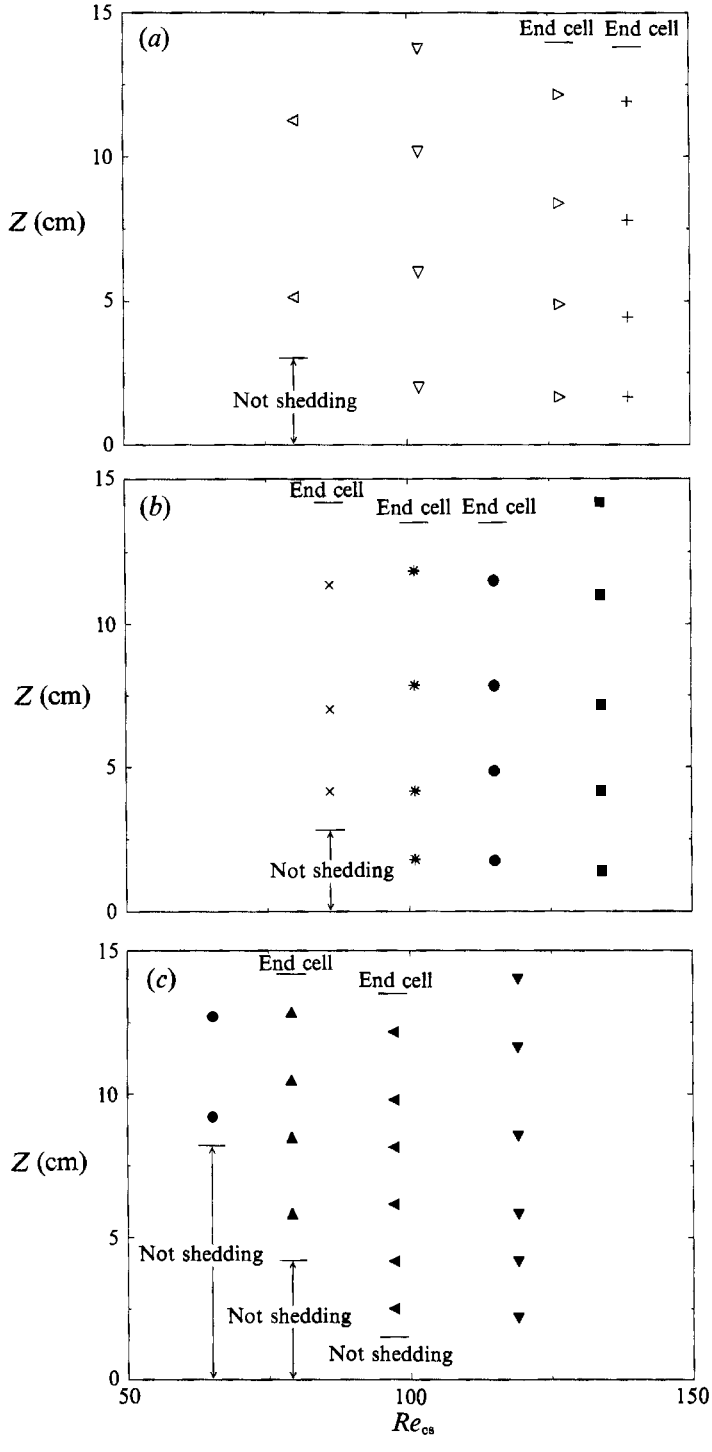

FIGURE 5. Cell midpoint locations for the 75:1, 60:1, and 50:1 cylinders, showing the creation of new cells. Areas not shedding and end cells are marked on the plots. (*a*) 75:1 cylinder: ◁, run 21; ▽, run 22; ▷, run 23; +, run 24. (*b*) 60:1 cylinder: ×, run 31; *, run 32; ●, run 33; ■, run 34. (*c*) 50:1 cylinder: ◆, run 41; ▲, run 42; ◀, run 43; ▼, run 44.

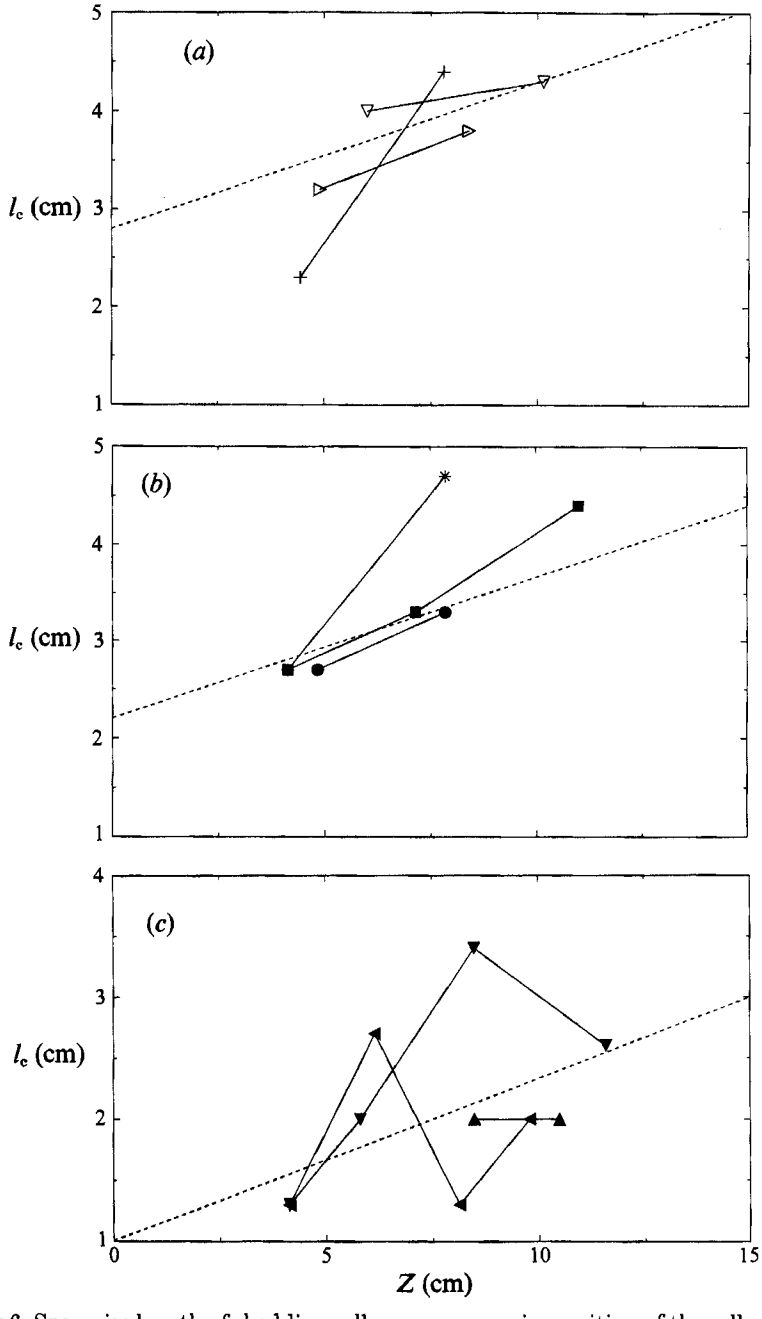

FIGURE 6. Spanwise length of shedding cells versus spanwise position of the cell midpoint. Symbols are the same as figure 5, with the dashed lines representing expected cell size if the cells follow the self-similarity hypothesis. (*a*) 75:1 cylinder; (*b*) 60:1 cylinder; (*c*) 50:1.

in Reynolds number across the cell ($\Delta Re_{\text{cell}} = Re_{\text{end 1}} - Re_{\text{end 2}} = U_0(d_{\text{end 1}} - d_{\text{end 2}})/\nu$) and then by dividing it by the centrespan Reynolds number to obtain

$$R_c = \frac{\Delta Re}{Re_{cs}} = \frac{d_i - d_j}{d_{cs}} = \frac{z_i - z_j}{R_T d_{cs}}.$$

Note that the taper ratio of the cylinder appears as a linear factor in the non-

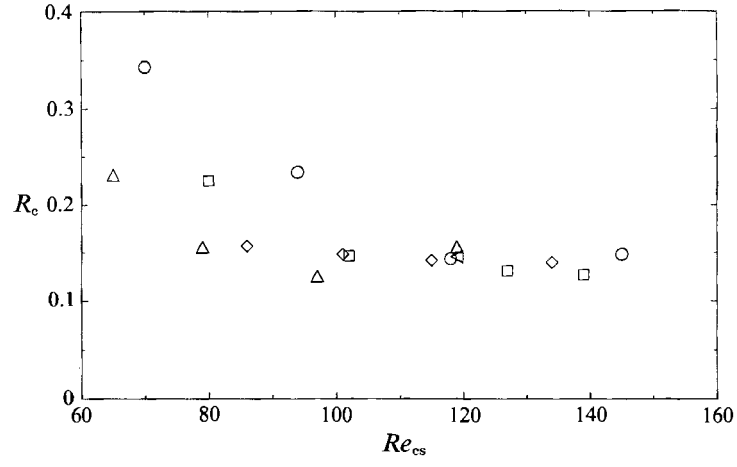

FIGURE 7. Non-dimensionalized cell size R_c plotted against Re_{cs} for all cylinders: ○, 100:1 cylinder; □, 75:1; ◇, 60:1; △, 50:1; ◁, data of Noack *et al.* (1991).

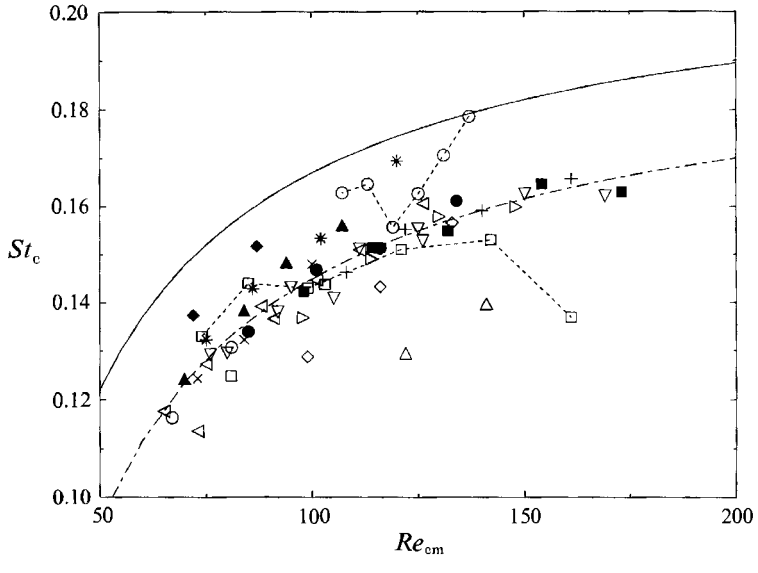

FIGURE 8. Cell Strouhal numbers versus cell midpoint Reynolds number: ○, run 11; □, run 12; ◇, run 13; △, run 14; ◁, run 21; ▽, run 22; ▷, run 23; +, run 24; ×, run 31; *, run 32; ●, run 33; ■, run 34; ◆, run 41; ▲, run 42; ◀, run 43; ▼, run 44; ○---○, data of Jespersen & Levit (1991); □---□, data of Noack *et al.* (1991); —, Roshko curve; – –, best-fit curve to the data.

dimensionalized cell length. R_c was plotted against centrespan Reynolds number for all the experiments. The results, given in figure 7, show a clear pattern. For low Re_{cs}, R_c depends directly on the taper ratio of the cylinder, i.e. the cylinder with the least amount of taper has the largest cell size. As Re_{cs} was increased, the R_c values for all the cylinders collapsed onto one line, for Re_{cs} values of 100 or more. The results of Noack *et al.*, also plotted in figure 7, show excellent agreement with the present results.

From figure 7, we can now see why the number of cells in each cylinder becomes

a constant, as shown in figure 4. As the Reynolds number increases, the mean cell length of the cylinder becomes a constant, thus 'freezing' the number of cells along the cylinder. Of more importance is the fact that the cell size collapses for all four cylinders. This suggests that the flows for all of the cylinders are very similar in their underlying structure, with the small amount of taper present affecting the cylinders in a purely linear fashion. The taper thus produces a purely geometric effect in determining the number of cells along the cylinder.

3.2. *Shedding frequencies*

A scaling of the vortex shedding frequencies was also investigated. For each cell, the primary shedding frequency was converted into a cell Strouhal number using the midpoint diameter of the cell, i.e.

$$St_c = fd_{\text{cell midpoint}}/U.$$

This Strouhal number was then plotted against the local Reynolds number, which was also calculated using the cell midpoint diameter. The results are shown in figure 8. The collapse of the data is excellent, and therefore we conclude that there is a universal Strouhal number versus Reynolds number curve, which is independent of taper ratio. Also shown in figure 8 are results from Noack *et al.* (1991), and the computational results of Jespersen & Levitt (1991). The results of Noack *et al.* generally compare well with the present results, while the computational Strouhal numbers are somewhat higher.

In figure 8, the Roshko (1954) Strouhal–Reynolds number curve for a straight cylinder is shown. It was hoped that Williamson's geometrical formula,

$$St_{\text{angle}} = St_{\text{parallel}} \cos(\theta),$$

could be used to fit the present data to the Roshko curve, thus allowing the calculation of an effective vortex shedding angle. However, the Strouhal curve for the tapered cylinders was found to be slightly steeper than that for a straight cylinder. We conjectured that the Strouhal curve might be steeper for tapered cylinders because the vortex convection velocity was not a constant along the span of the cylinder. To test this, the vortex convection velocities were measured for each of the cylinders. We found that the convection velocity for each cylinder was in fact constant along the span, with values of about $0.84U$ for the 50:1 cylinders, $0.86U$ for the 60:1 cylinder, and $0.80U$ for the 75:1 and 100:1 cylinders. Thus, it seems that the increased steepness of the Strouhal number curve is an intrinsic feature of tapered cylinders. The best-fit curve of the data was found to be

$$St_c = 0.195 - 5.0/Re.$$

This curve is similar in form to the Strouhal versus Reynolds number curve found by Roshko (i.e. $St = a - b/Re$), with the numerical constants differing by about 10%.

In his first tapered-cylinder paper (1969), Gaster pointed out that the onset Reynolds number of vortex shedding, Re_0, was postponed for his cylinders, from the usual value of about 40 for an untapered cylinder, to a local value of 57 in the case of a 36:1 cylinder, and 65 in the case of an 18:1 cylinder. Re_0 was estimated for all of our cylinders by calculating the Reynolds number for the diameter at which the spectral magnitude at the vortex shedding frequency became larger than the spectral magnitude of any noise in the system (60 Hz noise, for example). The results of this investigation are shown in figure 9, along with results from Van Atta & Piccirillo

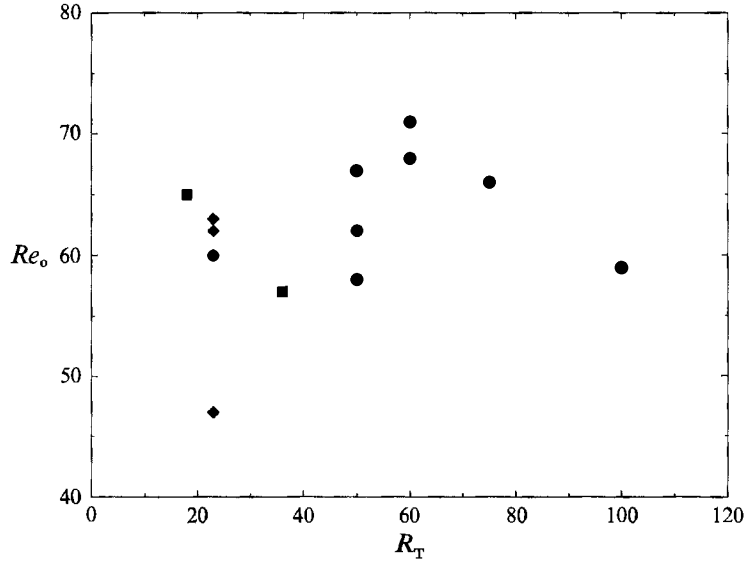

FIGURE 9. Onset Reynolds number of vortex shedding versus taper ratio: ●, present data; ■, data of Gaster (1969); ◆, data of Van Atta & Piccirillo (1990).

(1990). These results are consistent with Gaster's in the sense that the start of vortex shedding is delayed for all the cases examined, but in the present experiment no effect of taper ratio was found. This suggests that tapered cylinders begin shedding vortices at a Reynolds number of around 60 independent of other factors.

3.3. *Modulation frequencies*

Gaster (1969) suggests that the modulation frequency is a constant along the cylinder. This assertion was tested in all of our cases, by plotted the modulation frequency found at each cell boundary against the spanwise position at that cell boundary.

In figure 10, modulation frequency is plotted for all of our experiments in which the cylinder being tested had more than two shedding cells. The modulation frequency is roughly a constant along the span of the cylinder, although some cases show considerable scatter. It should also be pointed out that the resolution of the modulation frequency is limited in our experiments, as the bin size for the FFT was 0.135 Hz, or about 7% of the usual modulation frequency of around 2 Hz.

We attempted to generate a universal modulation frequency Strouhal versus Reynolds number curve which would include the effects of both taper ratio and flow speed. Since the modulation frequency was nearly constant along the span of the cylinders, it was scaled globally, against cylinder centrespan Reynolds number (Re_{cs}). The resulting Strouhal number was then modified to take into account the difference in taper ratios by using the following formula:

$$St' = \frac{fd_{\text{shedding midpoint}}}{U\sin(\theta)},$$

where the shedding midpoint is defined as the centre of that portion of the cylinder which is shedding vortices and $\theta = \tan^{-1}(1/R_T)$ is the taper angle of the cylinder. We are, in effect, proposing a decomposition of the flow into a part normal to the forward

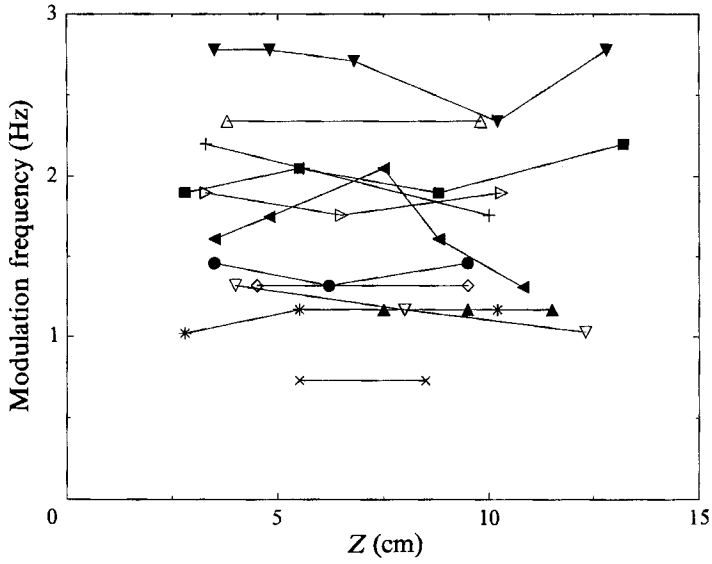

FIGURE 10. Modulation frequency for all runs with more than two shedding cells versus cell midpoint position. Symbols are the same as in figure 8.

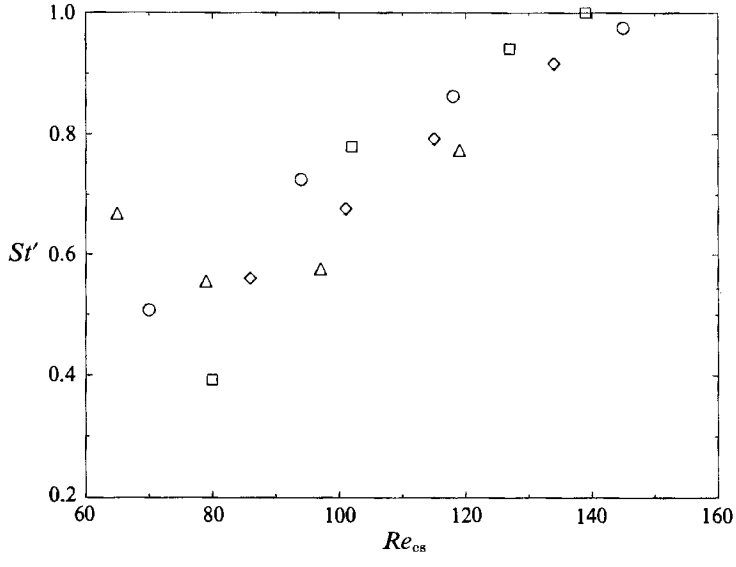

FIGURE 11. Modulation Strouhal number versus centrespan Reynolds number. Symbols are the same as in figure 7.

surface of the cylinder, which determines shedding frequencies, and a part parallel to the forward surface of the cylinder, which determines the modulation frequency. The geometry of the cylinder and the mean flow speed are both contained in this decomposition. As shown in figure 11, the data collapse very well, especially at the higher Reynolds numbers, similar to the results of the cell length scaling. This result suggests that the decomposition proposed above has physical validity in the flow, as using the component of the velocity parallel to the forward surface of the cylinder enables us to scale the modulation frequency, while the component normal to the

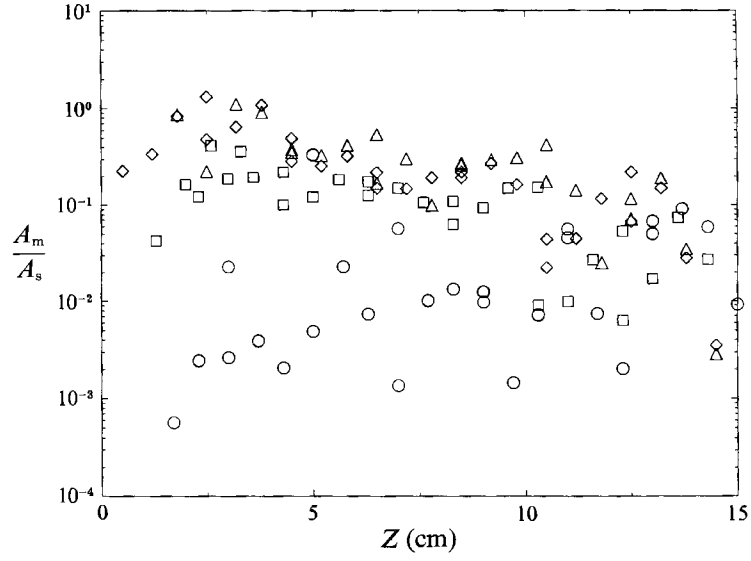

FIGURE 12. Ratio of the amplitude of the modulation frequency to that of the dominant shedding frequency versus spanwise position: ○, run 13; □, run 23; ◇, run 33; △, run 43.

forward surface of the cylinder (for which the correction factor, $\cos(\theta)$, is essentially 1) scales the shedding frequency. The decomposition also suggests that the modulation frequency is a constant along the cylinder, because it depends on the component of velocity parallel to the forward surface of the cylinder, which is itself a constant. The decomposition is also useful because it predicts that the amount of taper will affect the flow is a very simple way, which our results show.

The amplitude of the modulation frequency relative to the shedding frequencies was investigated for all the cylinders. The results are shown in figure 12, in which the amplitude of the modulation frequency, A_m, normalized by the primary shedding frequency, A_s, is plotted versus spanwise location. A_m/A_s is roughly independent of spanwise location; and A_m/A_s grows as the taper ratio decreases, although the increase is very small in the range $R_T = 75:1$ to $50:1$. The amplitude of the modulation frequency does not increase in strength at the cell boundaries. This is a somewhat surprising result, which suggests that the modulation frequency may be a more intrinsic function of the global flow than previously suspected, and that information about the modulation frequency is effectively transported spanwise along the entire cylinder by an overall (i.e. independent of spanwise position) flow process.

3.4. *Effect of different end conditions*

Figure 13 shows the locations of the cell boundaries for the 100:1 cylinder, with $U = 0.5$ m/s, for five different endplate configurations. The five configurations were: (i) large endplates on both ends of the cylinders, (ii) small endplates on both ends, (iii) 'nubs' on both ends, (iv) a nub on the small-diameter end and a large endplate on the large-diameter end, and (v) a nub on the large-diameter end and a large endplate on the small-diameter end. There is no consistent change in the locations of the cell boundaries with changing end conditions. The last two cases shown, each with a 'nub' at one end of the cylinder and a large circular endplate at the other, are especially interesting. These end conditions were chosen to create an additional unbalanced pressure condition on the cylinder similar to the type that produces

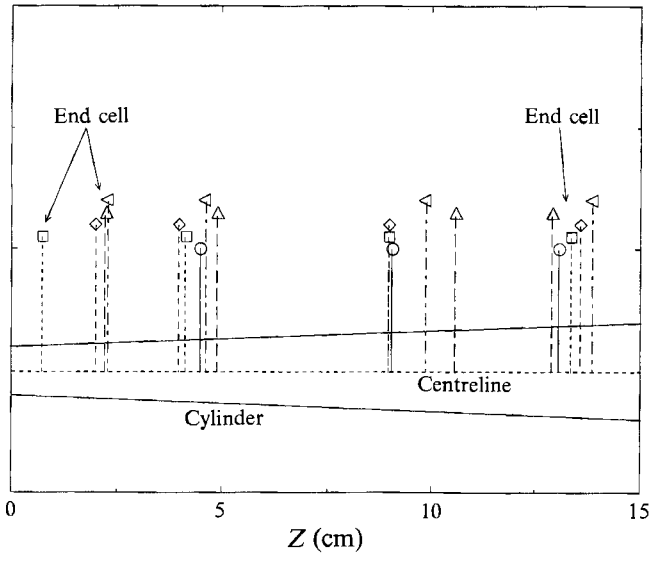

FIGURE 13. Cell boundary locations for 100:1 cylinder with a flow velocity of 0.5 m/s, for five different endplate configurations: ○—, large endplates on both ends; □---, nubs on both ends; ◇---, small endplates on both ends; △--, nub on small-diameter end, large endplate on large-diameter end; ◁---, nub on large-diameter end, large endplate on small-diameter end.

Position of endplate	Shedding length (cm)	Aspect ratio
3 cm from narrow end	12.2	35:1
6 cm from narrow end	9.2	26:1
9 cm from narrow end	6.2	17:1
3 cm from wide end	12.2	39:1
6 cm from wide end	9.2	31:1
9 cm from wide end	6.2	22:1
middle	7.6 (narrow side)	26:1
middle	7.6 (wide side)	21:1

TABLE 2. Configurations used in the variable-endplate experiments

oblique vortex shedding for a straight cylinder. Indeed, flow visualization showed that for these two end conditions, the non-tapered control cylinder did shed obliquely. However, even these extreme end conditions had no consistent effect on the tapered-cylinder cell boundary positions. The shedding frequencies in the flow were found to be invariant with respect to differing endplate configurations, and the flow visualization results yielded no detectable differences in the vortex shedding for different endplate configurations. The vortex shedding geometry of the flow is thus largely unaffected by end conditions.

3.5. *Effect of aspect ratio*

The effect of variable aspect ratio was tested in two ways. First, a movable end plate, 7.5 cm in diameter, was placed at several different spanwise locations along the cylinder, which are given in table 2. The flow was then examined to see how the endplate location affected the vortex shedding. The results of this investigation are given in figure 14. As the endplate was moved from the large-diameter end of the

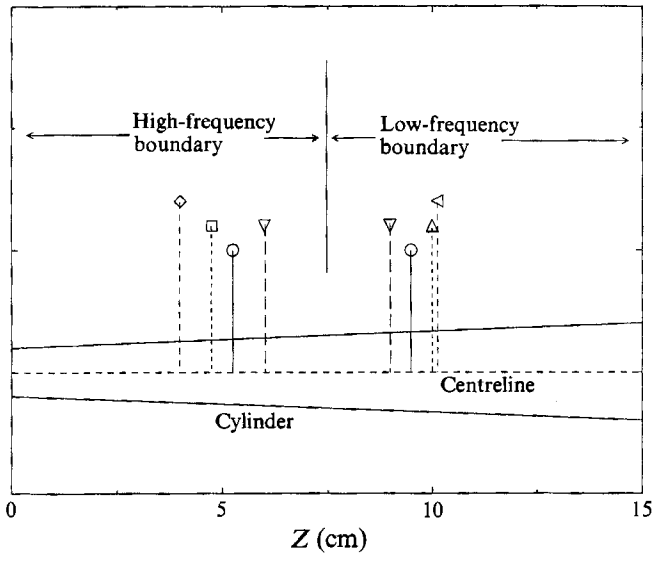

FIGURE 14. Cell boundary locations for 100:1 cylinder with a flow velocity of 0.5 m/s, showing the effect of variable endplate location: ○—, 3 cm from large-diameter end; □---, 6 cm from large-diameter end; ◇---, 9 cm from large-diameter end; △---, 3 cm from small-diameter end; ◁---, 6 cm from small-diameter end; ▽—, in middle of the cylinder.

cylinder towards the small-diameter end, the shedding frequencies in the flow did not change, nor did the modulation frequency, nor did the position of the cell boundary nearest to the endplate (until it was swallowed up by the endplate's boundary layer). The cell boundary further away from the endplate moved about 2 cm towards the small-diameter end. When the situation was reversed, with the variable endplate moving from the small-diameter end of the cylinder towards the large-diameter end, a similar scenario was observed. When the variable-position endplate was placed at the centrespan of the cylinder, both cell boundaries disappeared, being replaced by boundaries between the shedding cells and the end cells of the variable position endplate. These cells had approximately the same location as the previous shedding cell boundaries. These results show that changing aspect ratio does have an effect on the cylinder, but that this effect is small, as the cell size does not change, nor do the shedding or modulation frequencies. The main effect of the variable endplate was to change the flow in the endplate's immediate vicinity.

The second test of variable aspect ratio was done using the 50:1 taper ratio cylinder. The flow velocity for run 41 was chosen so that part of the cylinder was not shedding vortices. The mean speed was then systematically increased (which introduced a Reynolds number effect) and the cell boundary locations were determined. As previously seen in figure 5(*c*), one of the cell boundary locations moved between runs 41 and 42, but after that, the cell boundaries moved very little as the flow speed was increased. New cells were created in the region where before there had been no vortex shedding. There was no noticeable spanwise movement of vortex-shedding cells along the cylinder into the non-shedding region of the flow. On the contrary, the cell boundaries seem to move away from the non-shedding region of the flow as new cells were added. Thus, aspect ratio effects on the flow are small. Assuming that for high enough Re, the mean cell length is a constant for all the cylinders, we postulate that the effect of aspect ratio is essentially a linear one,

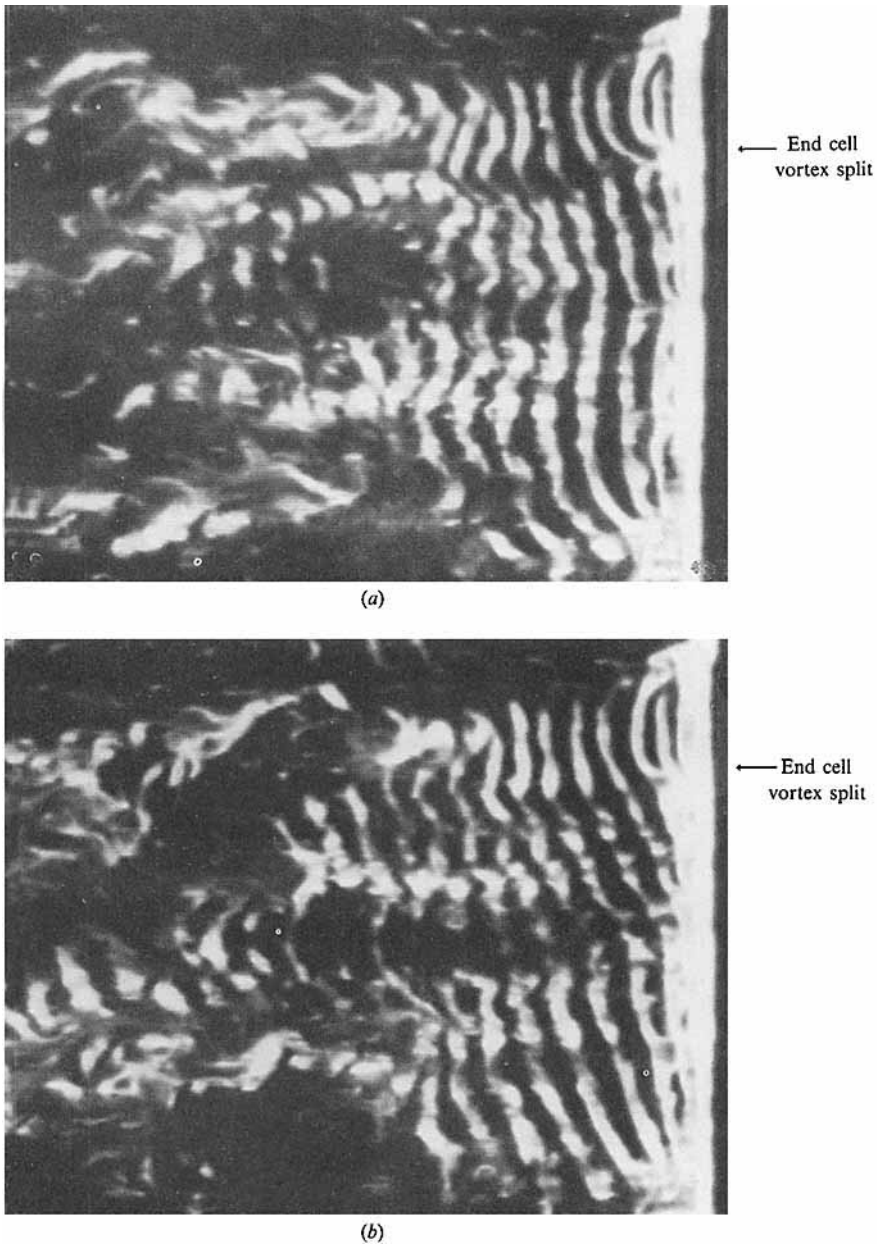

FIGURE 15(*a*, *b*). For caption see p. 181.

inducing no changes in any of the shedding or modulation frequencies in the flow, but adding new cells in direct proportion to the aspect ratio of the cylinder.

3.6. *Synchronization of the vortex splits*

Along with the overall flow pattern discussed above, the time behaviour of the flow was also studied, using water tunnel flow visualization. The constancy of the modulation frequency, both in frequency and in magnitude, and the decomposition of the flow discussed above, suggested that the vortex splits might be sequentially

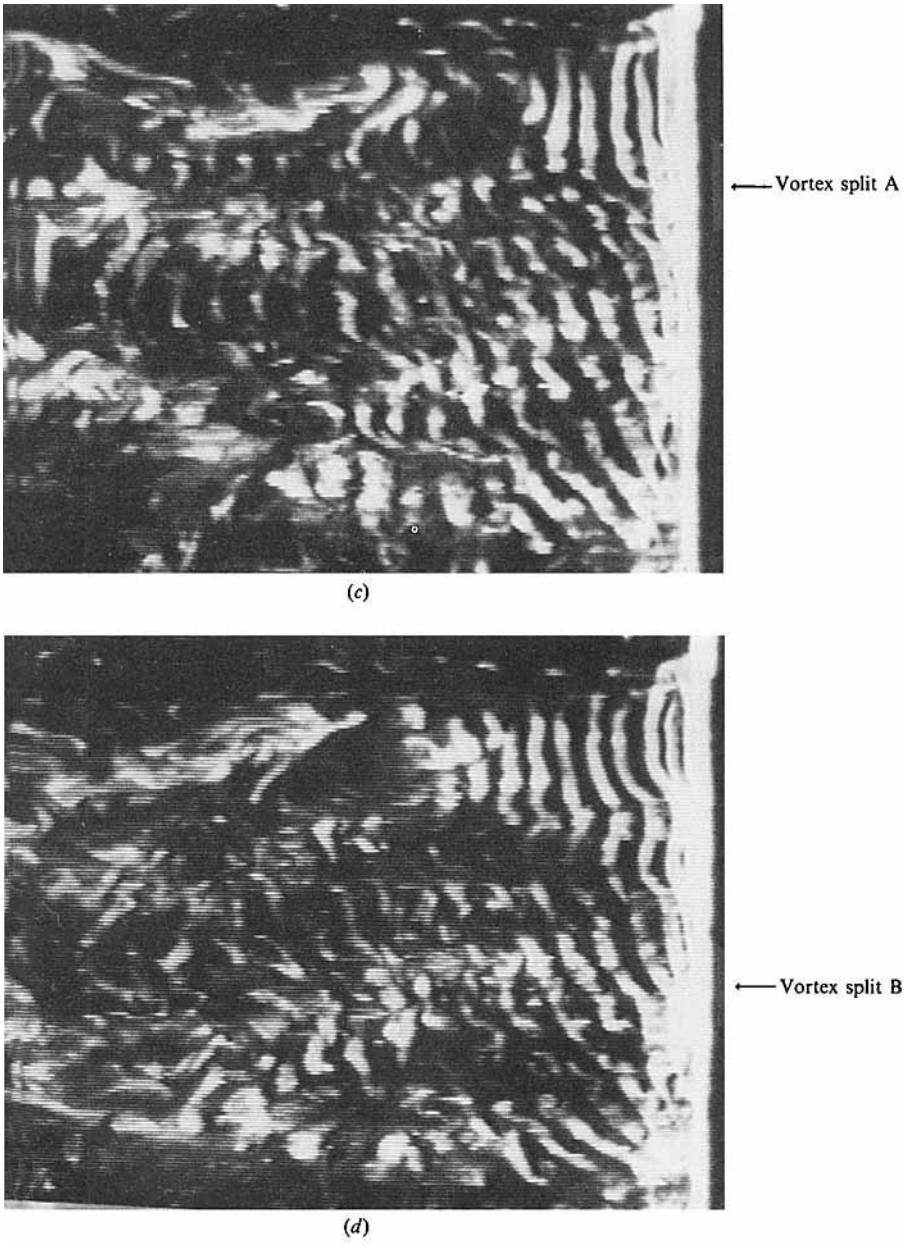

FIGURE 15(*c*, *d*). For caption see facing page.

linked spanwise along the cylinder. Therefore, the time behaviour of the overall flow was studied visually from the video of the water channel runs to see if it exhibited a consistent pattern of evolution. For the smallest three tapers, a clear pattern emerged for both the vortex shedding and the vortex splits. This pattern is illustrated in figure 15, beginning in figure 15(*a*) where the vortices are shedding nearly parallel to the cylinder, in a nearly continuous vortex line, save for an end-cell vortex split seen near the narrow end of the cylinder. Owing to the increased rate of shedding at the top of the cylinder, the vortex lines then begin to bend over, as shown in figure 15(*b*) (note that the end-cell vortex split can still be seen). It is

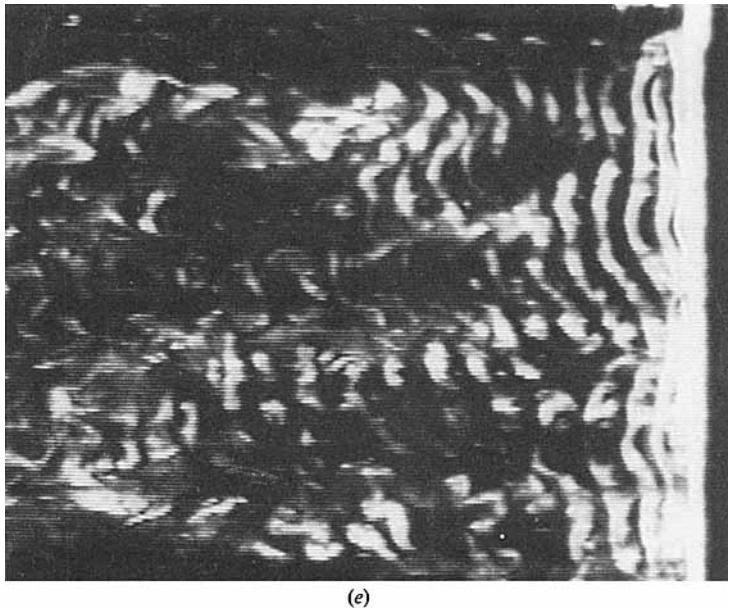

(*e*)

FIGURE 15. Time history of the cycle of vortex shedding behind the cylinder. (*a*) Initial state: vortex lines are continuous and nearly parallel to the cylinder centreline; (*b*) 2 s later: vortex lines are still continuous, but are now obliquely shed; (*c*) 1 s later: vortex splitting has begun, near the small-diameter end of the cylinder (top of the photograph); (*d*) 1 s later: vortex splitting continues, moving down the cylinder; (*e*) 1 s later: vortex splitting finished, the initial state reappears.

interesting to note here that no vortex splits have yet occurred. As the vortex lines continue to steepen, a vortex split finally occurs, near the small-diameter end of the cylinder, as shown in figure 15(*c*). The vortex splits then occur in succession, moving from the small-diameter end of the cylinder to the large-diameter end. After the last split, which occurs near the large-diameter end of the cylinder (shown in figure 15*d*), the vortex lines once again become continuous and aligned nearly parallel to the cylinder, as shown in figure 15(*e*), and the cycle begins again.

The behaviour for the 50:1 cylinder, however, was not so well ordered. At no time was a continuous vortex line being shed by the cylinder. Also, the vortex splits themselves did not follow the small- to large-diameter pattern described above. This is probably due to the large number of cells, and hence the large number of vortex splits, which occur too frequently in time to allow for continuous vortex lines to be shed at any time. The steepening of vortex lines observed for the other three cylinders did occur here, but the process was somewhat unclear, with an overall steepening of the vortex lines accompanied by continuous, evenly spaced in time, vortex splitting.

For the 100:1, 75:1, and 60:1 cylinders, the regular pattern allowed estimates to be made of the angle between the shed vortices and the cylinder axis. At the beginning of the cycle described above, this angle varied from $+5°$ to $-5°$, with a mean of nearly zero. The maximum angle before vortex splitting occurred was 20–30°, with a mean of about 25°. Once the vortex splits began, the vortex lines far away from the splits continued to steepen, reaching angles of 35°–55° (although this high an angle was rarely found). For the 50:1 cylinder, only local estimates of the shedding angle could be made, which were found to have the same range as the angles found for the other cylinders.

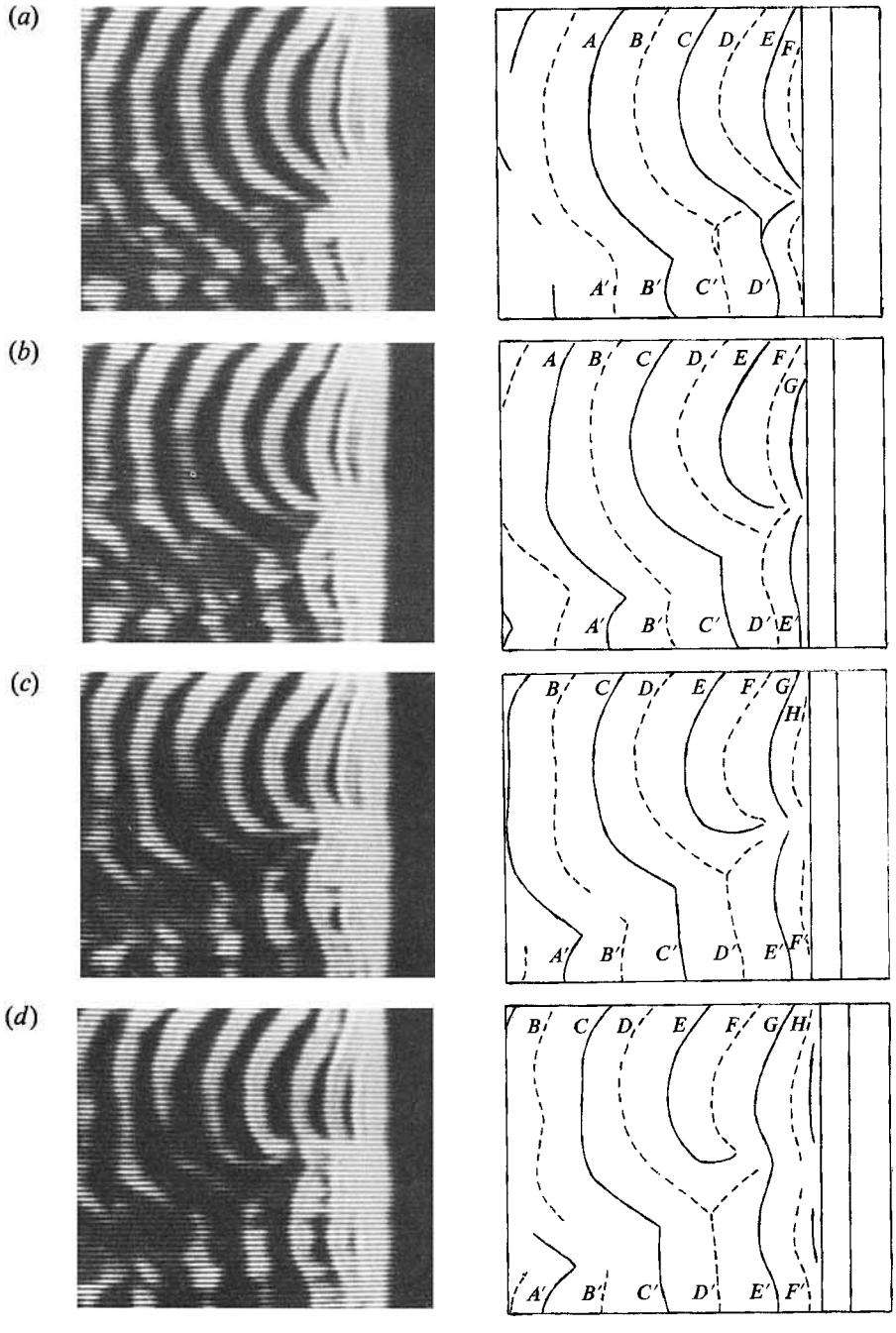

FIGURE 16(*a–d*) Time history of a vortex split. Line drawings are shown to aid the reader. Note that in the drawings, one side of the vortex street is illustrated with a solid line, the other with a dashed line.

3.7. *Vortex split geometry*

A series of four photographs which follow the development of a vortex split is shown in figure 16. Each photograph is accompanied by a line drawing in order to aid the reader. In the first photograph, the vortex splitting process has begun. This is

signalled by the formation of a kink in the vortex line being shed by the cylinder. The onset of the split is also evident on the lower-frequency side, where the shed vortex line (labelled B′) has left a filament connected to the cylinder. By the next photograph (figure 16*b*), the kink has deepened to the point where two shed vortex lines (labelled E and F) are connected to one another. As these two vortex lines move downstream, they remain connected to one another, as seen in figure 16(*c*). Finally, the vortex lines move away from the cylinder, still connected to one another (figure 16*d*). The 'loop' that is formed is similar to that seen by Lewis & Gharib (1992) for flow behind a stepped cylinder. Around this loop can also be seen vortex filaments from the lower vortex line (labelled D′) connecting both to the vortex line in front of the loop (labelled D) and the cylinder. This rear filament eventually breaks free of the cylinder and attaches itself to the rear vortex line of the loop (labelled F). After this complex split, the kink in the vortex lines disappears and the flow returns to shedding straight vortex lines in this region until the angle of shedding becomes too steep and the cycle begins again. This process is very similar to that seen by Williamson (1989) behind a straight cylinder, except that the present split ends in a cross-street connection. The reason for this difference is not clear.

The development of the kink in the vortex lines is preceded by a slight bulge in the vortex lines, as if a perturbation of some sort was being imposed on the vortex line. This, together with the fact that vortex splitting occurs after the shedding angle has reached some critical angle, suggests that there is a secondary instability in the flow, which occurs when the angle of shedding becomes too great, or put another way, when the amount of streamwise vorticity becomes too large.

In figure 17(*a*), the vortex splitting process is shown with the laser sheet intersecting the cylinder at an angle of 90° with respect to the cylinder centreline, i.e. at a constant spanwise location. The connection of one vortex line to another on the other side of the vortex street at the vortex split can be clearly seen in first photograph, which is similar to flow visualization results of Gaster (1969). This is compared to the normal shedding pattern shown in figure 17(*b*).

Another interesting aspect of the vortex shedding pattern was the occurrence of large holes, where no dye was present, in the regions where the vortex split occurred. These can be seen in figures 15 and 16, occurring directly behind the cylinder. The holes seen here are similar to the ones seen by Williamson (1991), which he connects with the existence of three-dimensionality in the wake of a non-tapered cylinder. From the flow visualization in figure 16, the hole can be seen as starting at the kink in the vortex lines. This suggests that the discontinuity in streamwise vorticity at the kink, where the two vortex lines come together at different angles, creates the hole by advecting dyed fluid out the kink region. Three-dimensionality in the wake is concentrated here due to the high velocity shear in this region, which is caused by both the vorticity discontinuity and the stretching of the vortex lines which are still attached to the cylinder. As the hole convects downstream, its effects diffuse out, eventually affecting the entire wake.

Having looked qualitatively at the topology of the vortex split using flow visualization, we next turn to looking at it quantitatively. Our hot-wire anemometry experiments showed, as expected, that the spanwise location of the vortex split is in the region in which the cell boundary was detected using spectral methods. Thus, the vortex split is the vortex dynamical connection across the cell boundary described spectrally in §3.1. In addition to the visualization evidence presented above, the vortex split signature can be seen in comparative velocity plots, such as the one shown in figure 18. The two velocity traces are from adjacent measuring stations

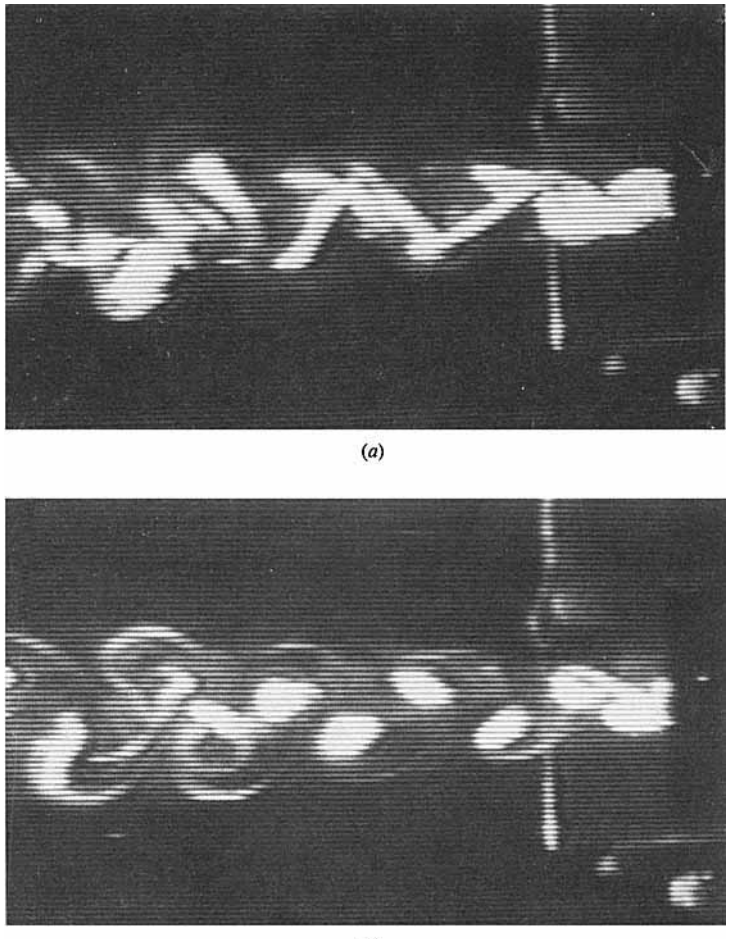

(a)

(b)

FIGURE 17. Side view of the vortex shedding, showing (a) a vortex split with the observed cross-wake connections, and (b) the normal vortex shedding pattern (note that these two photographs were taken at the same spanwise location).

which are on opposite sides of a cell boundary region (vortex split). At the peak of the modulation, where the fluctuation in the signal has been reduced to almost zero, there are two peaks (marked x) in the high-frequency-cell velocity trace corresponding to only one peak (marked y) in the lower-frequency-cell velocity trace. At this point, the phase difference between the two signals, as seen in the phase difference versus time plot shown in figure 19, is approximately 180°.

Comparing the phase differences in figure 19 with the vortex split photograph shown in figure 16, we see that the phase relationship between signals on opposite sides of the cell boundary is qualitatively consistent with the vortex line configuration around the vortex split. The phase of the higher-frequency-cell vortex lines, being closer together in space, moves forward relative to the lower-frequency-cell vortex lines until they are about 180° 'ahead' in phase, at which point a vortex split occurs, and the vortex lines are able to realign themselves to be roughly in phase again. The bending of the vortex lines around the vortex split caused by the kink structure can be clearly seen in figure 16. To investigate this phenomenon more closely, the time

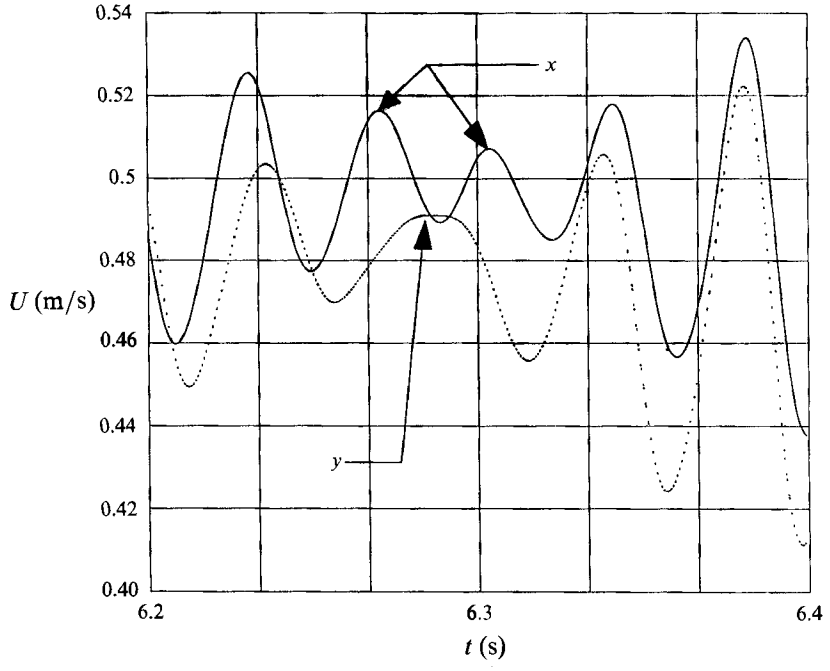

FIGURE 18. Comparative velocity time trace at two adjacent measuring stations, on opposite sides of a cell boundary, as a vortex split occurs. Note the two peaks marked by x, which correspond to one peak, marked by y, in the other signal. —, $Z = 4.5$ cm; ..., $Z = 4.9$ cm.

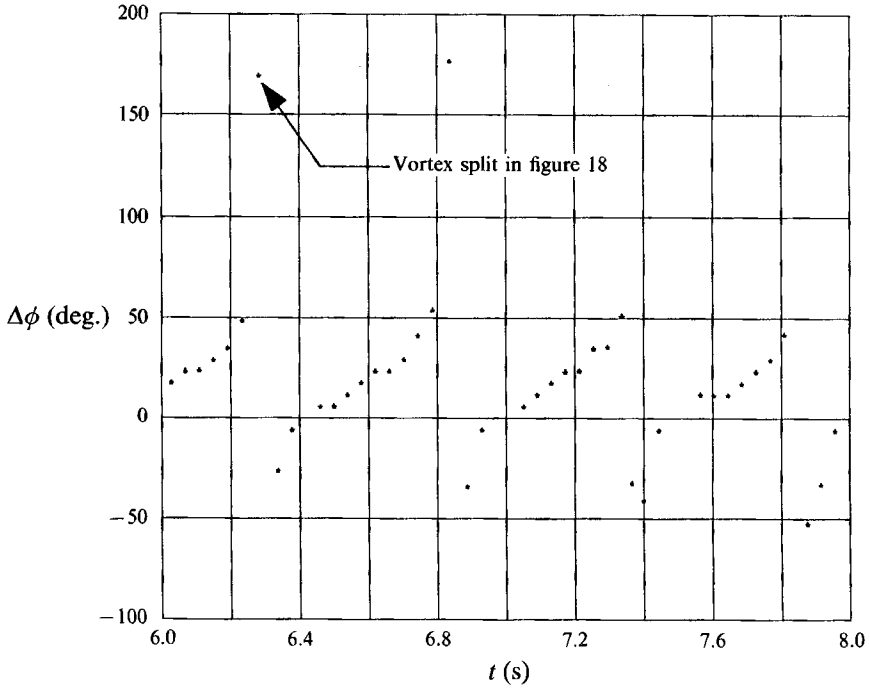

FIGURE 19. Comparative phase between the two signals shown in figure 18. Note that the two signals are 18° out of phase when a vortex split occurs.

between adjacent peaks of a hot-wire signal taken near the vortex split was investigated. The time between the peaks represents, when multiplied by the drift velocity, the spatial distance between the vortex lines. The distance between the vortex lines was found to change by up to 20% near the vortex split. This is indicative of the vortex lines bending to accommodate the split. This bending of lines is a process distinct from the increasing of the angle of the vortex lines shown in figure 15, as it only occurs near the vortex split. Further away from the split (1.5 cm away for the 100:1 cylinder), the distance between the vortex lines is a constant. This increase in the distance between the vortex lines can also be thought of as a decrease in local frequency, as inverting the time between peaks will lead to the generation of a local frequency. Therefore, the bending of vortex lines around the vortex split leads to a decrease in the local frequency of vortex shedding.

3.8. *Amplitude results*

In order to clarify how the vortex split appears in space, the spatial distribution of its influence was investigated, using two techniques. In the first, the Hilbert transform

$$\widetilde{x(t)} = \int_{-\infty}^{\infty} \frac{x(u)}{\pi(t-u)}\,\mathrm{d}u,$$

where $x(u)$ is the original data set, was applied to the velocity data. The magnitude of the resulting complex time series, $\widetilde{x(t)}$, represents the amplitude of the velocity fluctuations. The variation of this amplitude in time in the region around the vortex split allows us to study its topology in detail. Figure 20 plots the magnitude for the region around one vortex split in run 23. In the plot, one set of data from a rake of four wires is used. A cubic interpolation scheme was used to create the contours for the plot. The maximum amplitude in the record was normalized to 1. There is an elliptically shaped amplitude 'hole' around the vortex split, which is marked by L (for low point). The 'hole' extends much further in the spanwise direction than in the downstream direction, and is aligned at an angle of roughly 25° to the cylinder centreline. This is a different picture than that obtained by Dallard & Browand (1993), who found a nearly circular 'hole' around the vortex split in a plane shear layer. In this case, the influence of the vortex split on the flow is very large in the spanwise direction, indicating that spanwise communication along the span of the cylinder is a very important part of the overall picture of the flow. This result is in agreement with our conjectures in §§3.3 and 3.6, based on the modulation frequency results, and the coherent timing of the vortex splits. The plot shown here is typical of those for all of the cylinders, suggesting that despite the lack of order in the vortex splitting found in the flow visualization for the 50:1 cylinder, the overall flow structure for this cylinder is similar to that for the other three.

The exact nature of this structure is, at this time, somewhat unclear. However, given the results of Hammache & Gharib (1989), who showed that oblique shedding behind a straight cylinder led to both a pressure gradient and a flow along the base of the cylinder, as well as our earlier decomposition of the flow into parts normal and parallel to the cylinder, it seems likely that the structure of the flow that sequentially connects all of the vortex splits and transports information about the modulation frequency is a pressure gradient (and its associated flow) along the base of the cylinder. The pressure gradient is caused by the pressure difference between the two ends of the cylinder, due to their differing diameters.

To investigate the effect of taper ratio on the vortex splits, the Hilbert transform

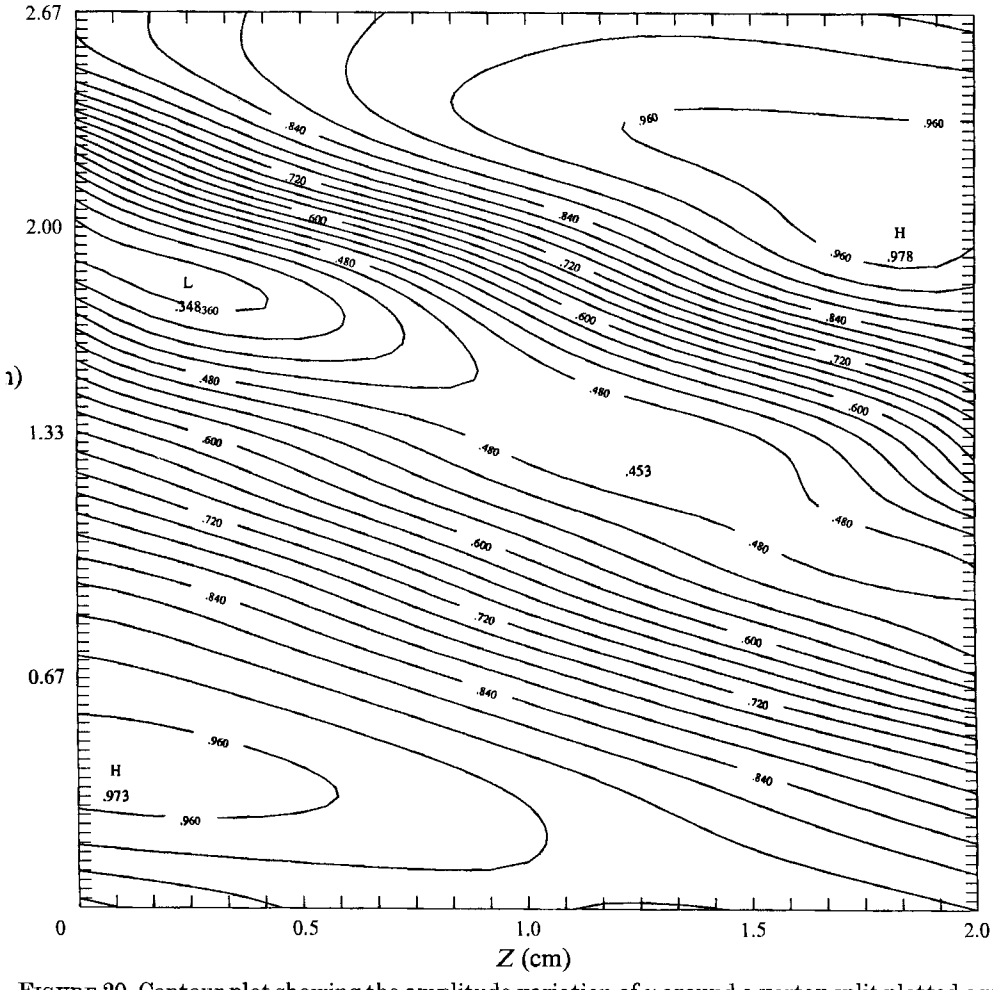

FIGURE 20. Contour plot showing the amplitude variation of u around a vortex split plotted against spanwise and downstream position. This particular split was taken from run 23, and is typical of results from all the other runs. Note that $Z = 0$ in the figure corresponds to $Z = 6.3$ cm on the cylinder.

amplitude results were plotted for long times. The results are shown in figure 21. There is a noticeable difference between the amplitude function of the 100:1 cylinder (figure 21*a*), which has extended amplitude peaks, and those for the other three cylinders, which have a more sinusoidal behaviour. Also, for the three smallest tapers, the maximum magnitude of the amplitude is approximately the same for each peak. For the 50:1 cylinder, the maximum magnitude of the amplitude varies by more than 30% from cycle to cycle, and the close correspondence between the four signals making up the plot is broken at certain locations. The reason for this may be that other vortex splits along the cylinder are affecting the magnitude of the signal at the chosen location. We note that the velocity-time-trace amplitude variations found for this cylinder are more similar in shape to those found in the more steeply tapered cylinders used by Van Atta & Piccirillo (1990) and by Gaster (1969).

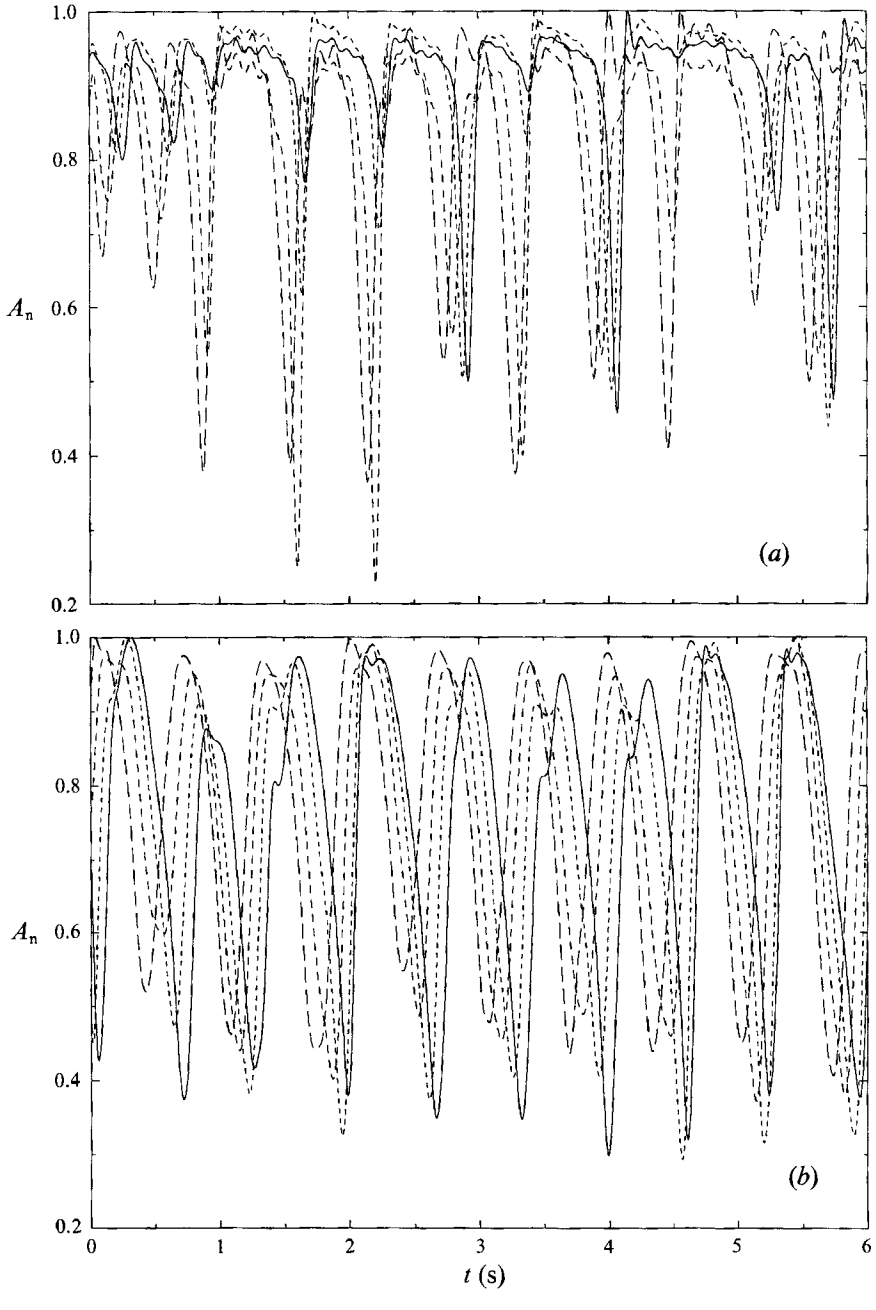

FIGURE 21 (a, b). For caption see facing page.

3.9. *Wavelet analysis*

In order to further our topological studies of the vortex split, as well as get more information about the modulation frequency, wavelet analysis was applied to selected data sets. The wavelet analysis used employed the Morlet wavelet (Liandrat & Moret-Bailly 1990):

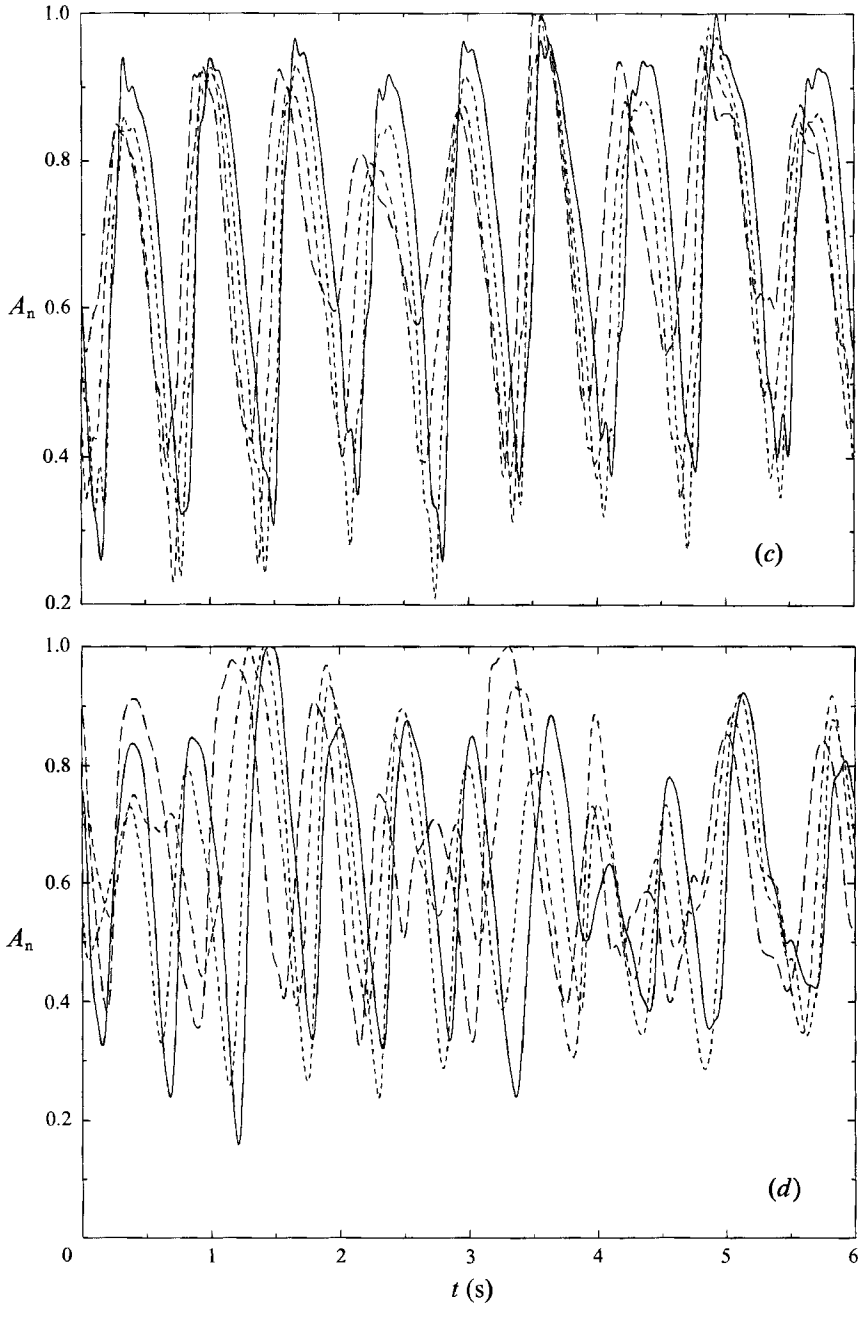

FIGURE 21. Variation in the normalized amplitudes of four simultaneous signals plotted for long times: (*a*) run 14, —, $Z = 6.0$ cm; ..., $Z = 6.7$ cm; ---, $Z = 7.3$ cm; – –, $Z = 8.0$ cm. (*b*) run 23, —, $Z = 6.3$ cm; ..., $Z = 7.0$ cm; ---, $Z = 7.6$ cm; – –, $Z = 8.3$ cm. (*c*) run 33, —, $Z = 8.5$ cm; ..., $Z = 9.2$ cm; ---, $Z = 9.8$ cm; – –, $Z = 10.5$ cm. (*d*) run 43, —, $Z = 6.5$ cm; ..., $Z = 7.2$ cm; ---, $Z = 7.8$ cm; – –, $Z = 8.5$ cm.

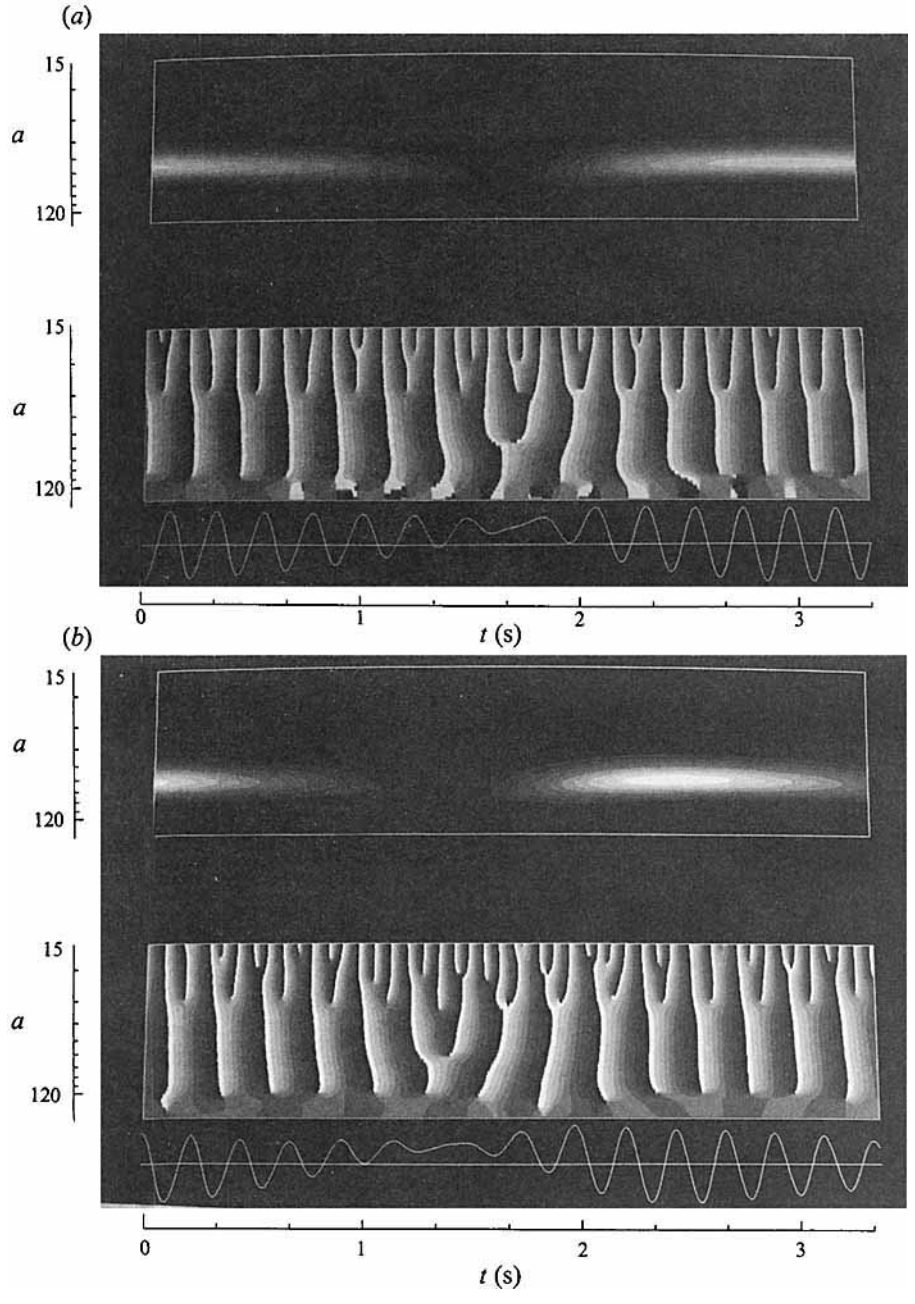

FIGURE 22. Wavelet results for scales corresponding to the shedding frequencies. In both (*a*) run 23, and (*b*) run 43, the scale parameter a for the plots ranges from 15 to 120, corresponding to frequencies of 87 down to 11 Hz. In both plots, magnitude is plotted at the top of the figure, phase in the middle, and the signal which was transformed at the bottom. Each grey shade corresponds to 10% of the maximum value computed for the plot.

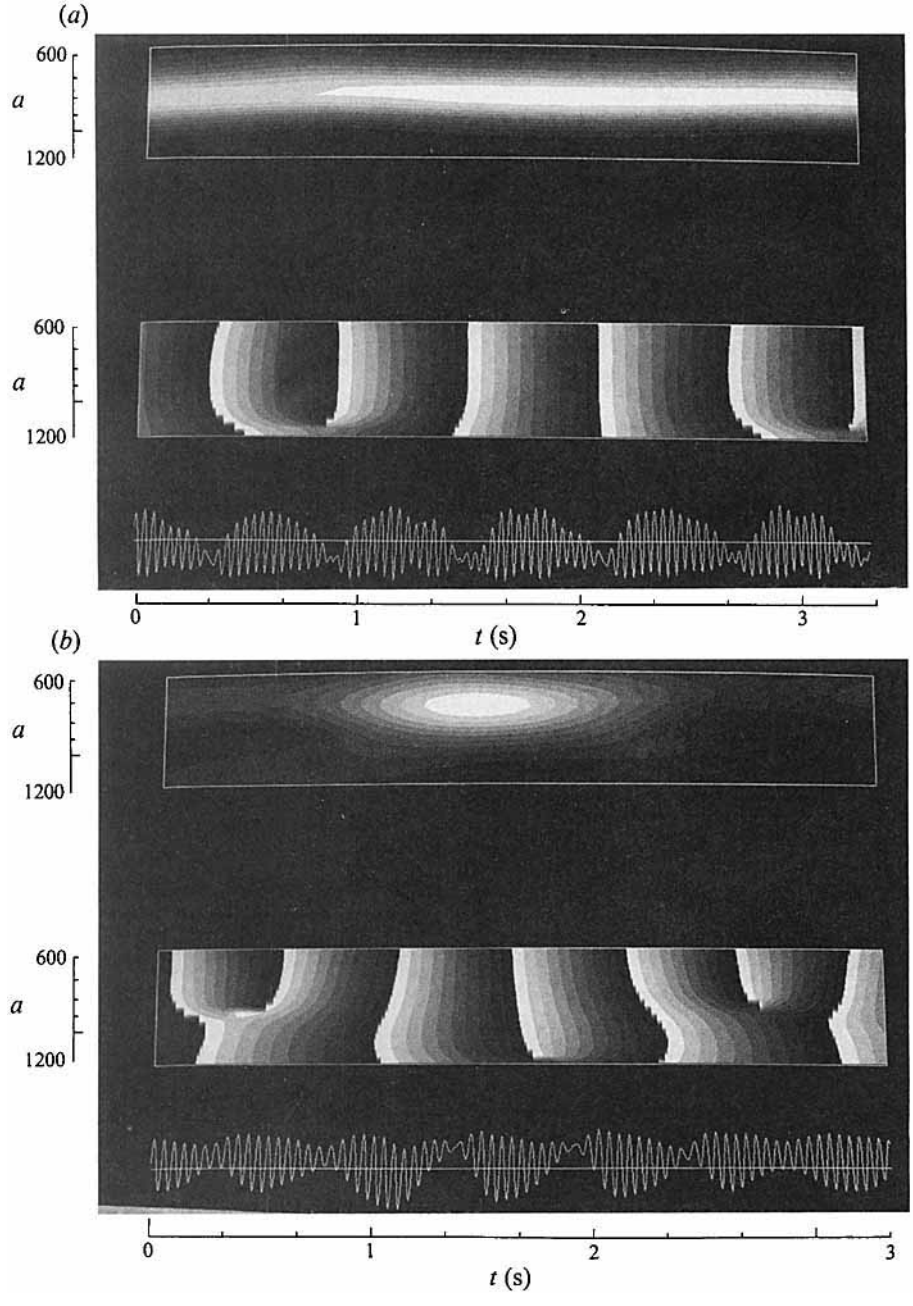

FIGURE 23. Wavelet results for scales corresponding to the modulation frequencies. In both (*a*) run 13, and (*b*) run 43, the scale parameter a for the plots ranges from 600 to 1200, corresponding to frequencies of 2.2 down to 1.1 Hz. The set-up and grey scales used are the same as in figure 22.

$$g\left(\frac{x'-x}{a}\right) = \exp\left(\mathrm{i}k_0\frac{x'-x}{a}\right)\exp\left(-\frac{(x'-x)^2}{2a^2}\right),$$

where a and k_0 are parameters, the former defining the scale of the wavelet (and thus inversely its frequency), and the latter defining the number of cycles of the complex exponential. For all the results discussed here, k_0, which is dimensionless, was set to

5.5. The Morlet wavelet was used because, being complex, it gives separable magnitude and phase information for the flow. In figure 22, we plot the wavelet analysis results at scales near the shedding frequency scale for the signals plotted at the bottom of the figures, for the 75:1 cylinder in figure 22(*a*), and the 50:1 cylinder, in figure 22(*b*). The magnitude plots recapture the amplitude holes that were also seen in the Hilbert transform analysis. The slight downward curving of the magnitude isocontours around the vortex split indicates a reduction in the local shedding frequency, confirming the previous results which showed the local frequency decreasing near the vortex split.

From the phase plots, we can clearly see both the shedding frequencies and their first harmonics evolving as the flow evolves toward a vortex split. The harmonics of the shedding frequencies, which are initially arranged in a consistent pattern, break from this pattern as the vortex split approaches. The split then occurs, coming into existence only at scales near the shedding frequencies and at smaller scales. The harmonics then reorganize themselves as the flow further evolves in time. As seen from the plots, this harmonic variation was found to depend little on the taper ratio.

Similar plots of results of wavelet analysis performed at scales close to the modulation frequency scale are shown in figure 23. The magnitude plot shows a much larger qualitative difference than the shedding frequency results. For the 100:1 cylinder (figure 23*a*), the magnitude of the modulation frequency changes by less than 20% over the course of the plot (which represents 3.33 s of time), and the phase lines are well ordered. In figure 23(*b*), by contrast, the magnitude of the 50:1 cylinder modulation frequency is a strong function of time, losing 90% of its value over the course of the plot. The phase information is also much less organized. The 75:1 and 60:1 cylinder results were similar to those of the 100:1 cylinder, although both had greater amplitude changes (around 40% for both).

These results, together with the Hilbert transform results, suggest that the flow behaviour for the 50:1 cylinder, while being characterized similarly in the mean to the other three cylinders, is, upon closer examination, somewhat less ordered. The velocity signals found for the 50:1 cylinder appear very similar to those of Van Atta & Piccirillo (1990) and Gaster (1969). For cylinders with taper ratios between 13:1 and 32:1, Van Atta & Piccirillo found a 'leaky' cellular structure, in which non-adjacent shedding cells can effect one another significantly. Our present 50:1 cylinder appears to have the same sort of structure. The other three cylinders, for which the flow is much more ordered, might then be thought of as having a 'tight' cellular structure, whereby non-adjacent cells do not significantly affect one another. It is significant that the primary differences between the two flows are found in the behaviour of the modulation frequency. The modulation frequency can therefore be viewed not as a passive part of the overall flow, but an active one, which is very much responsible for both the overall and the detailed behaviour of the flow.

4. Comparison with other results

4.1. *Comparison with non-tapered-cylinder results*

In the non-tapered-cylinder studies of Gerich & Eckelmann (1982), Eisenlohr & Eckelmann (1989), and Williamson (1989), so called 'end cells' are discussed at length. Of specific interest here is the vortex splitting process by which the end cells connect themselves to the primary shedding cell. Vortex splits from Williamson, Eisenlohr & Eckelmann, and the present work were compared. The splits show an interesting difference, in that in the present case, the splits formed *across* the vortex

street, while in Williamson's case, the split seems to connect vortex lines on the same side of the vortex street. It is unclear at this time whether this difference is a fundamental one, implying that the physics of the split is different in the two cases, or an incidental one, in which the physics in the two flows is similar, but with some difference of detail (perhaps flow uniformity). The other similarities in the vortex splits, especially the development of the 'kink' in the vortex line at the split, and the persistence of a trailing element of vorticity reaching back to the cylinder from the shed vortex lines, suggest that the difference is an incidental one.

A comparison between adjacent-cell phase relation plots of Williamson's data and the present data (figure 19) shows excellent qualitative agreement. The strong similarities between these results, as well as the results of Maull & Young, Browand & Troutt, etc. cited in the introduction, suggests that the vortex splitting process is a generic vortex dynamics connection mechanism between frequency-mismatched vortex shedding regions, which can occur under a wide variety of conditions.

4.2. *Comparison with other non-uniform-cylinder results*

We began our comparison with earlier tapered-cylinder results in §3.8, where we compared velocity plots from Gaster (1969), Van Atta & Piccirillo (1990), and the present work. As discussed there, the 50:1 cylinder data look very similar to the results presented by these earlier researchers, while the data for the other cylinders looked somewhat more organized. Good qualitative agreement was found in a comparison of the velocity spectra of Van Atta & Piccirillo and the spectra for all of the cylinders used in the present work.

The results of Noack *et al.* (1991) are also in good agreement with ours. As shown above, the cell size scaling proposed here collapsed their data and ours onto the same curve. Their cell size behaviour is similar to what we have found, i.e. the shedding cells not adjacent to the cylinder ends increased in size move from the small- to the large-diameter end of the cylinder. Their results also support our conjecture concerning the linearity of the effect of aspect ratio, as their $R_T = 90:1$ cylinder has six cells for an aspect ratio of 90:1, while our 100:1 cylinder has three cells for an aspect ratio of 47:1. Also of great interest for comparison are the results of the numerical simulation of Jespersen & Levit (1991), which was designed to closely model our experiment. Their flow visualization results, velocity time traces, cell length, and cell boundary placements show great similarities with the present results. However, as shown in the Strouhal number versus Reynolds number plot (figure 8), their shedding frequencies are in poor agreement with our results. Also, near the large-diameter end of their cylinder, the numerical simulation showed a breakdown to complex turbulent-like velocity spectra, which may indicate a computational problem.

Lewis & Gharib (1992) speculate that for cylinders with a small amount of taper, the vortex splitting process is governed by local interactions, and thus will be similar to their direct mode interaction, while for larger taper, the cylinder will behave globally, similar to their indirect mode interaction. The primary indication of the indirect mode, and thus a way to distinguish the two modes, is that the vortex split, as it develops in time, will move spanwise along the cylinder. From figure 16, we see that the vortex split moves towards the narrow end of the cylinder as it occurs, indicating that in this aspect, the vortex splits of Lewis & Gharib's indirect mode resemble the present ones. The vortex splits of their indirect mode are also similar to the present results in the behaviour of the relative phase of two signals on opposite sides of the split. In both cases, the phase of the higher-frequency signal moves

forward relative to the lower-frequency signal until it is about 180° out of phase, at which point the vortex split occurs. The vortex splits of Lewis & Gharib's indirect mode are thus similar to those found here. In none of our results did we find a vortex split that resembles the Lewis & Gharib direct mode split.

5. Conclusions

The primary effect of taper is to produce vortex splits, or dislocations. These vortex splits begin with a secondary instability in the flow, which leads to a kink in the shed vortex lines. This kink deepens and moves towards the narrow end of the cylinder, eventually leading to a cross-street splitting event. Amplitude analysis suggests that the splits are sequentially linked, a suggestion borne out in the timing of the splits for the three lowest tapers. The mechanism underlying this process may involve the pressure gradient along the span of the cylinder. Wavelet analysis shows that the harmonics of the shedding frequency are affected by the split, and that for higher amounts of taper, the behaviour of the modulation frequency becomes much less ordered. This behaviour gives velocity signals very similar in form to those seen by Gaster (1969) and Van Atta & Piccirillo, suggesting that two regimes of taper exist, one with a 'tight' cell structure, and one with a 'leaky' cell structure.

The cell size for all of the cylinders can be successfully scaled for centrespan Reynolds number greater than 100. The number of cells for these Reynolds numbers is a linear function of the degree of taper (which is equal to $1/R_T$). The number of cells is also a linear function of the aspect ratio of the cylinder. The dimensionless shedding frequencies collapse onto one curve for all the cylinders without any explicit accounting for the different taper ratios. The modulation frequency was also scaled successfully, by including the effects of Reynolds number and taper ratio. These two scalings suggest that the effect of taper ratio on the overall flow is approximately linear for low values of R_T.

This study was partially supported by DARPA grant number N00014-86-K-0758 and by the University of California under an INCOR grant with the Center for Nonlinear Studies at Los Alamos National Laboratory. We thank Dr Gary Doolen of CNLS for useful discussions and for encouragement of both experimental and computational efforts on this problem.

The authors would also like to thank Christine Lewis for many helpful discussions and for making a copy of her manuscript available to us before publication. We would also like to thank Bernd Noack for making his manuscript available to us before publication. Helpful discussions with Dr Dennis Jespersen of NASA-Ames, Professor Fred Browand of USC, and Professor Charles Williamson of Cornell are also acknowledged.

REFERENCES

Browand, F. K. & Prost-Domasky, S. 1990 Experiment on pattern evolution in the 2-D mixing layer. In *New Trends in Nonlinear Dynamics and Patterning Phenomena: The Geometry of Non Equilibrium* (ed. P. Coullet & P. Huerre). Plenum.

Browand, F. K. & Troutt, T. R. 1985 The turbulent mixing layer: geometry of large vortices. *J. Fluid Mech.* **158**, 489–509.

Dallard, T. & Browand, F. K. 1993 The growth of large scales at defect sites in the plane mixing layer. *J. Fluid Mech.* (in press).

EISENLOHR, H. & ECKELMANN, H. 1989 Vortex splitting and its consequences in the vortex street wake of cylinders at low Reynolds numbers. *Phys. Fluids* A **1**, 189–192.

GASTER, M. 1969 Vortex shedding from slender cones at low Reynolds numbers. *J. Fluid Mech.* **38**, 565–576.

GASTER, M. 1971 Vortex shedding from circular cylinders at low Reynolds numbers. *J. Fluid Mech.* **46**, 749–756.

GERICH, D. & ECKELMANN, H. 1982 Influence of end plates on the shedding frequency of circular cylinders. *J. Fluid Mech.* **122**, 109–121.

GRIFFIN, O. 1987 Vortex shedding from bluff bodies in shear flow: A Review. *Trans. ASME* J: *J. Fluids Engng* **107**, 298–306.

HAMMACHE, M. & GHARIB, M. 1989 A novel way to promote vortex shedding in the wake of circular cylinders. *Phys. Fluids* A **1**, 1611–1614.

JESPERSEN, D. & LEVIT, C. 1991 Numerical simulation of flow past a tapered cylinder. *AIAA 29th Aerospace Sciences Meeting, Reno, AIAA Paper* 91–0751.

LEWIS, C. G. & GHARIB, M. 1992 An exploration of the wake three dimensionalities caused by a local discontinuity in cylinder diameter. *Phys. Fluids* A **4**, 104–117.

LIANDRAT, J. & MORET-BAILLY, F. 1990 The wavelet transform: some applications to fluid dynamics and turbulence *Eur. J. Mech.* B *Fluids* **9**, 1–19.

MAULL, D. J. & YOUNG, R. A. 1973 Vortex shedding from bluff bodies in shear flow. *J. Fluid Mech.* **60**, 401–409.

NOACK, B. R., OHLE, F. & ECKELMANN, H. 1991 On cell formation in vortex streets. *J. Fluid Mech.* **227**, 293–308.

PICCIRILLO, P. S. 1990 An experimental study of flow behind a linearly tapered cylinder at low Reynolds number. M.S. thesis, University of California, San Diego.

ROSHKO, A. 1954 On the development of turbulent wakes from vortex streets. *NACA Rep.* 1191.

SLAOUTI, A. & GERRARD, J. H. 1981 An experimental investigation of the end effects of the wake of a circular cylinder towed through water at low Reynolds numbers. *J. Fluid Mech.* **112**, 297–314.

VAN ATTA, C. W. & PICCIRILLO, P. 1990 Topological defects in vortex streets behind tapered circular cylinders at low Reynolds numbers. In *New Trends in Nonlinear Dynamics and Patterning Phenomena: The Geometry of Non Equilibrium* (ed. P. Coullet & P. Huerre), pp. 243–250. Plenum.

WILLIAMSON, C. H. K. 1989 Oblique and parallel modes of shedding in the wake of circular cylinders at low Reynolds numbers. *J. Fluid Mech.* **206**, 579–627.

WILLIAMSON, C. H. K. 1991 The natural and forced formation of 'vortex dislocations' in the transition to three-dimensionality of a wake. *Bull. Am. Phys. Soc.* **36**, 2629.

WOO, H. G., CERMAK, J. E. & PETERKA, J. A. 1989 Secondary flows and vortex formation around a circular cylinder in constant-shear flow. *J. Fluid Mech.* **204**, 523–542.